TU Delft

Delft University of Technology

Document Version
Final published version

Licence
CC BY

Citation (APA)
Yarali, E., Staufer, U., Fratila-Apachitei, L. E., Al-Sanea, A., Mahdavi, R., Zadpoor, A. A., Accardo, A., & Mirzaali, M. J. (2026). Decoupling mechanical and morphometric properties in meta-biomaterials. *Nature Communications*, *17*(1), Article 9359. https://doi.org/10.1038/s41467-026-77121-y

Important note
To cite this publication, please use the final published version (if applicable).
Please check the document version above.

Copyright
In case the licence states “Dutch Copyright Act (Article 25fa)”, this publication was made available Green Open Access via the TU Delft Institutional Repository pursuant to Dutch Copyright Act (Article 25fa, the Taverne amendment). This provision does not affect copyright ownership.
Unless copyright is transferred by contract or statute, it remains with the copyright holder.

Sharing and reuse
Other than for strictly personal use, it is not permitted to download, forward or distribute the text or part of it, without the consent of the author(s) and/or copyright holder(s), unless the work is under an open content license such as Creative Commons.

Takedown policy
Please contact us and provide details if you believe this document breaches copyrights.
We will remove access to the work immediately and investigate your claim.

*This work is downloaded from Delft University of Technology.*

nature communications

Article

https://doi.org/10.1038/s41467-026-77121-y

# Decoupling mechanical and morphometric properties in meta-biomaterials

Received: 18 October 2024

Accepted: 7 August 2026

Published online: 08 September 2026

Check for updates

Ebrahim Yarali[1,2] ✉, Urs Staufer[2], Lidy E. Fratila-Apachitei[1], Abdulrahman Al-Sanea[1], Reza Mahdavi[3], Amir A. Zadpoor[1,4], Angelo Accardo[2,4] ✉ & Mohammad J. Mirzaali[1,4] ✉

A significant challenge in developing meta-biomaterials is the effective decoupling of their intrinsically intertwined mechanical properties (*e.g.*, elastic and shear moduli, Poisson's ratio, and anisotropy level), morphometric properties (*e.g.*, relative mass density, pore size, and surface-to-volume ratio), and mass-transport properties (*e.g.*, permeability). To address this challenge, we introduce a general framework for decoupling mechanical and morphometric properties in non-stochastic, three-dimensional meta-biomaterials. We first derived explicit geometrical relationships to determine the upper and lower bounds of the input geometrical parameters while ensuring relevance to in vitro biological conditions. Using a high-throughput numerical homogenization method (44,837 simulations) combined with systematic multi-objective optimization, we successfully decoupled Poisson's ratio and relative mass density from all other properties, with average deviations below ~14%. The optimized meta-biomaterials were additively manufactured at the macro- and microscales using PolyJet 3D printing and two-photon polymerization, respectively, and experimentally validated in terms of effective elastic modulus, Poisson's ratio, and permeability. The established decoupling framework provides a promising route for advancing tissue engineering and cell mechanobiology studies by enabling independent investigation of the effects of individual scaffold properties on cell behavior.

Meta-biomaterials are a class of engineered, biocompatible materials whose unique properties originate not from their compositions but from their micro-architectural design. These architected materials offer a wide design space for real-world applications, particularly in biomedical engineering, enabling functionalities beyond those achievable with conventional biomaterials. For example, structures with negative Poisson's ratios, so-called auxetics, have been demonstrated to offer mechanical responses not common in natural tissues[1–5].

The fundamental building blocks of meta-biomaterials can be stochastic or deterministic, and are often constructed from either strut-based[6–9] or surface-based unit cells[10,11]. The architectural design and spatial arrangement of these unit cells provide unprecedented freedom in tuning a wide range of physical properties. This flexibility enables simultaneous control of mechanical (e.g., elastic modulus, Poisson's ratio, Zener ratio), morphometric (e.g., porosity, pore size, tortuosity), and mass-transport properties (e.g., permeability, diffusivity)[3].

[1]Department of Biomechanical Engineering, Faculty of Mechanical Engineering, Delft University of Technology, Delft, the Netherlands. [2]Department of Precision and Microsystems Engineering, Faculty of Mechanical Engineering, Delft University of Technology, Delft, the Netherlands. [3]Department of Industrial Engineering, BIOtech - Center for Biomedical Technologies, University of Trento, Trento, Italy. [4]These authors jointly supervised this work: Amir A. Zadpoor, Angelo Accardo, Mohammad J. Mirzaali ✉e-mail: E.yarali@tudelft.nl; A.Accardo@tudelft.nl; M.J.Mirzaali@tudelft.nl

Well-established relationships govern many of these properties. For instance, the effective elastic modulus scales with relative density following a power-law relation[12], bounded by the Hashin-Shtrikman theoretical limits[13]. Similarly, permeability correlates with porosity and is further influenced by the pore morphology[12]. Poisson's ratio ($\upsilon$) in isotropic 3D solids is theoretically constrained between −1.0 and 0.5, corresponding to limits of bulk and shear moduli, as described by the relation $B/G = (\upsilon+1)/3(0.5-\upsilon)$, assuming positive values for both $B$ (i.e., bulk modulus) and $G$ (i.e., shear modulus)[12]. Within these bounds, specific classes of meta-biomaterials have reached extreme values of Poisson's ratio, e.g., penta-mode meta-biomaterials with 0.5[14], and auxetic designs with −1[15,16], However, achieving independent control over multiple mechanical parameters, such as simultaneously tuning Young's modulus and Poisson's ratio[17], remains a major challenge.

A critical limitation in current designs is the inherent interdependence among mechanical, morphometric, and mass-transport properties. Modifying one parameter, such as increasing stiffness, often alters others, like Poisson's ratio or permeability. For biomedical applications, particularly those aiming to replicate specific tissue environments or to isolate mechanobiological cues, it is essential to decouple these properties[18]. This challenge is even more pronounced when targeting extreme property values. For instance, designing meta-biomaterials with highly auxetic responses often introduces undesirable mechanical anisotropy, especially in non-stochastic 3D unit cells[19]. Therefore, geometric symmetry (e.g., with two[1] or three symmetry planes[20]) and mechanical isotropy (e.g., isotropic or cubic symmetry with minimal independent elastic constants) are highly desirable, particularly for mechanobiological investigations where directionality of cellular response matters[21].

The ability to independently tune Poisson's ratio, while keeping other properties constant, is especially relevant for applications, such as (hip) meta-implants[22] and mechanobiological studies of pre-osteoblasts[1], fibroblasts[21], and human mesenchymal stem cells[23]. While previous studies have explored the effects of Poisson's ratio on cellular behaviors, these investigations often involved 2D systems[23,24], nearly-zero values[20], or anisotropic responses across directions[1,23], without fully decoupling Poisson's ratio from other material properties. A systematic methodology to decouple individual mechanical and morphometric properties in 3D scaffold designs has yet to be established, despite its potential for biomedical research.

Several computational approaches have been employed to design meta-biomaterials with specific target properties. These include direct finite element (FE) simulations[25], homogenization-based FE methods[26], inverse design through physics-informed deep learning[3,27–29], and multi-objective optimization techniques[20,30]. Each method involves trade-offs between computational cost, precision, and scalability. Homogenization-based simulations[31] offer high efficiency for exploring large design spaces, and when combined with optimization algorithms, can enable property decoupling in a systematic manner. Previous studies have applied such frameworks to improve isotropy in auxetic materials[20] or balance stiffness and anisotropy through multi-objective design[30].

In this study, we propose a comprehensive design framework for creating 3D non-stochastic meta-biomaterials with tunable and decoupled mechanical, morphometric, and mass-transport properties. Our overall objective is to minimize the degree of interconnectivity between meta-biomaterials properties, including Poisson's ratio ($\upsilon$), effective elastic modulus ($E_{eff}$), effective shear modulus ($G_{eff}$), Zener ratio ($A$, anisotropy level), relative mass density ($\bar{\rho}$), pore size ($PS$), permeability ($k$), tortuosity ($\tau$), surface-to-volume ratio ($S/V$), and topological connectivity ($Z_g$). Using homogenization-based FE analysis, we systematically explored the design space and identified critical geometrical input parameters (e.g., strut length and orientation) that influence each property. A general multi-objective optimization strategy was also employed to achieve property decoupling with high computational efficiency.

To validate our numerical approaches, we fabricated the optimized 3D meta-biomaterials using two different additive manufacturing (AM) technologies, namely PolyJet and two-photon polymerization (2PP). Experimental characterization was performed at multiple length scales to assess their mechanical ($E_{eff}$, $\upsilon$) and permeability properties. Our results offer a scalable and systematic approach for the rational design of meta-biomaterials with independently tunable properties. We hypothesize that this decoupling framework will enable biomedical researchers to isolate and quantify the individual effect of mechanical and morphometric properties of scaffolds on cellular behavior. This ultimately accelerates the development of optimized scaffolds for tissue engineering applications, such as the study of the isolated effect of Poisson's ratio or relative mass density on the mechanobiological behavior of cells.

## Results and discussion

Herein, we first mathematically explored the design space of 3D non-stochastic meta-biomaterials, enabling the systematic generation of a wide range of possible designs (Fig. 1, Table 1, Supplementary Fig. 1 and Supplementary Table 1). Subsequently, we discuss the numerical modeling of the generated meta-biomaterials and their experimental validation, with the aim of achieving decoupled mechanical properties in meta-biomaterials.

### Optimizing voxel resolution for the homogenization of the meta-biomaterials

The mechanical behavior of meta-biomaterials is highly sensitive to the quality and resolution of voxelization, particularly when sharp geometrical features or overlapping struts are present. This sensitivity is especially pronounced in unit cells from Categories I and III, where extreme angles (e.g., $\theta \cong \theta_{\min}$ in Category I and $\theta \cong \theta_{\max}$ in Category III) lead to strut intersections. Capturing such geometric details with high fidelity requires higher voxel resolutions, but this significantly increases computational runtime. In some cases, accurate representation may necessitate voxel counts exceeding $n \geq 200$. Therefore, identifying an optimal voxel resolution that balances accuracy and computational efficiency is essential.

To determine a resolution suitable for the entire design space, we selected three representative unit cells: one critical case from Category I, an intermediate case from Category II, and one challenging case from Category III (see Supplementary Fig. 2 and Supplementary Table 2 for more details). Since these designs are among the most sensitive to voxelization, achieving property convergence for them would ensure adequacy for the remaining, less demanding unit cells.

We varied the number of voxels per strut, $n$, from $n_{\min} = 40$ to $n_{\max} = 460$, 340, and 360, in Categories I, II, and III, respectively (see Supplementary Table 2 for more details). For the three representative unit cells with different strut diameters ($d$) and assessed their mechanical properties (i.e., $\upsilon$, $E_{\text{eff}}/E_0$, $G_{\text{eff}}/G_0$ and $A$) for each $n$ (Supplementary Fig. 2 and Supplementary Table 2). Convergence was evaluated based on the relative variation in the properties between consecutive values corresponding to successive $n$ values, calculated as: $V = \left|X_{n_{i+1}} - X_{n_i}\right| / \left|X_{n_i}\right| \times 100$, where $X$ denotes a given property of interest.

The critical unit cell from Category I converged at $n = 340$ with a relative variation below 10.0%. In contrast, the unit cell from Category II reached convergence at $n = 200$, and the Category III unit cell at $n = 140$, both within a 5.0% threshold. These results confirm that Category I unit cells, with smaller $\theta$ and greater geometric complexity, require the highest $n$ for convergence.

Notably, using low voxel resolutions (e.g., $n < 80$), especially in the unit cells with thin struts, led to excessively coarse geometries

https://doi.org/10.1038/s41467-026-77121-y

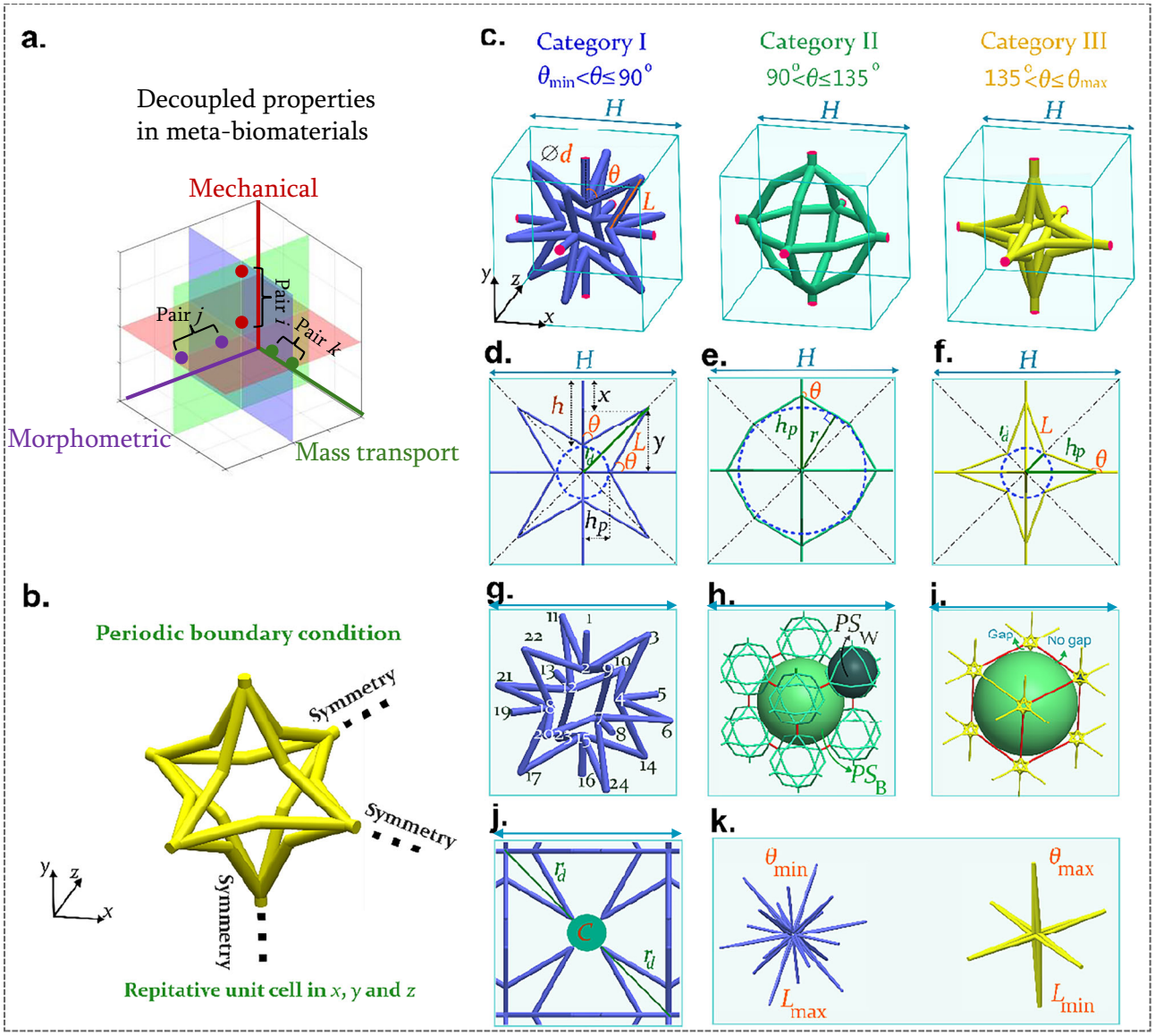



**Fig. 1 | Schematic showing the design process and geometrical constraints of the 3D non-stochastic meta-biomaterials. a** A general illustration of the objective of this study, showing the idea of decoupling of mechanical, morphometric and mass-transport properties in 3D meta-biomaterials. Pairs *i*, *j* and *k* are three symbolic pairs (two decoupled meta-biomaterials) with decoupled mechanical, morphometric, and mass-transport properties, respectively. **b** A schematic drawing of a parametrized 3D unit cell of the meta-biomaterial in a Cartesian coordinate system, with three planes of geometrical symmetry and periodic boundary conditions. **c** The classification of unit cells into three distinct categories: Category I ($\theta_{min} < \theta \leq 90.0^o$, shown in blue), Category II ($90.0^o < \theta \leq 135.0^o$, shown in green), and Category III ($135.0^o < \theta < \theta_{max}$, shown in yellow). Here, $\theta$, $L$ and $d$ are the three input parameters, while $H$ represents the overall size of the unit cell. **d** A 2D schematic drawing of a Category I unit cell, used to calculate parameters $h$, $h_p$, and $PS_W$. **e** A 2D schematic drawing of a Category II unit cell, illustrating the calculation of $PS_W$. **f** A 2D schematic drawing of a Category III unit cell, also used to calculate $PS_W$. **g** A 3D schematic showing a unit cell with labeled nodes. These labels are necessary for reporting their coordinates and morphometric properties. **h** A 3D schematic drawing of 2 × 2 × 2 unit cells (from Category II) demonstrating $PS_W$ and $PS_B$ **i** A 3D schematic showing $PS_B$ when $L$ is small enough that the green sphere does not touch the non-boundary struts but touches the red struts (boundary ones). **j** A 2D schematic representation illustrating the derivation of an explicit formula for the maximum $L$ in the unit cells of Category I. **k** A general schematic showing the critical unit cells of our developed meta-biomaterials with $\theta = \theta_{min}$, $L = L_{max}$, $d = d_{min}$ (the purple one) and with $\theta = \theta_{max}$, $L = L_{max}$, $d = d_{min}$ (the yellow one).

(Supplementary Fig. 2d, e.g., $n = 40$), and property variations exceeding 200%, demonstrating their inadequacy for reliable homogenization.

However, the computational cost escalates rapidly with $n$ and $d$ (or relative mass density). For instance, at $n = 200$, a unit cell with $d/H = 30.0/300$ required 50× more simulation time than one with $d/H = 8.0/300$. Likewise, increasing $n$ from 70 to 220 for a unit cell with $\theta = 171.7^\circ$, $L/H = 118.1/300$ and $d/H = 25.0/300$ resulted in a 200× increase in simulation time. Given the scale of this study (~44,837 simulations), optimizing computational efficiency was essential.

Considering both convergence behavior and computational cost, we selected $n = 200$ as the optimal voxel resolution for all meta-biomaterial simulations. At this resolution, the maximum variation in mechanical properties across the selected unit cells remained acceptable, which was 9.20% for shear modulus (Category I), 4.53% for shear modulus (Category II), and 2.65% for elastic modulus (Category III) (Supplementary Table 2).

**Table 1 | A summary of the final explicit geometrical relationships in our developed meta-biomaterials classified under Categories I, II and III**

| Category | Category I | Category II | Category III |
|---|---|---|---|
| $\theta$ | $\theta_{min}<\theta \leq 90^{o}$ | $90^{o}<\theta \leq 135^{o}$ | $135^{o}<\theta<\theta_{max}$ |
| $L$ | $0<L \leq 0.5H$ | $0<L \leq 0.36H$ | $0<L \leq 0.36H$ |
| $PS_W$ | $2L(\sin\theta-\cos\theta)-d$ | $2L\left(\sin^2\theta-\sin\theta\cos\theta\right)-d$ | $2L\sqrt{\sin^2\theta-\cos^2\theta+1}-d$ |
| $PS_B$ | $\min\left(\sqrt{2}H-d\&\sqrt{3H^2+8L^2\sin^2\theta-8HL\sin\theta}-d\right)$ | $\min\left(\sqrt{2}H-d\&\sqrt{3H^2+8L^2\sin^2\theta-8HL\sin\theta}-d\right)$ | $\min\left(\sqrt{2}H-d\&\sqrt{3H^2+8L^2\sin^2\theta-8HL\sin\theta}-d\right)$ |
| $PS_{min}$ | $2d$ | $2d$ | $2d$ |
| $L_{min}$ | $PS_W=PS_{min}$ | $PS_W=PS_{min}$ | $PS_W=PS_{min}$ |
| $L_{min}$ | $\frac{2d}{2(\sin\theta-\cos\theta)}$ | $\frac{2d}{2(\sin^2\theta-\sin\theta\cos\theta)}$ | $\frac{2d}{2\sqrt{\sin^2\theta-\cos^2\theta+1}}$ |
| $L_{max}$ | $\sqrt{2}H=2r+d+C$ | $h=h_{min}=d/2$ | $h=h_{min}=d/2$ |
| $L_{max}$ | $\frac{\sqrt{2}(H-d)}{2\sqrt{\sin^2\theta-\cos^2\theta+1}}$ | $\frac{H/2-d/2}{\lvert\sin\theta-\cos\theta\rvert}$ | $\frac{H/2-d/2}{\lvert\sin\theta-\cos\theta\rvert}$ |
| $\theta_{critical}$ | $L_{min}=L_{max}$ | – | $L_{min}=L_{max}$ |
| $\theta_{min}$ | $(d+PS_{min})\left(2\sqrt{\sin^2\theta_{min}-\cos^2\theta_{min}+1}\right)$ $-\sqrt{2}(H-d)(2(\sin\theta_{min}-\cos\theta_{min}))=0$ | – | – |
| $\theta_{max}$ | – | – | $\left(\frac{H}{2}-\frac{d}{2}\right)\left(2\sqrt{\sin^2\theta_{max}-\cos^2\theta_{max}+1}\right)$ $-(d+PS_{min})(\lvert\sin\theta_{max}-\cos\theta_{max}\rvert)=0$ |

## Mechanical properties of the meta-biomaterials

We systematically explored the mechanical design space of the developed meta-biomaterials by analyzing how their effective properties vary with the strut angle ($\theta$) and normalized strut length ($L/H$), (Fig. 2a and Supplementary Fig. 3a–d). The evaluated mechanical properties include $\upsilon$, $A$, normalized effective elastic modulus ($E_{eff}/E_0$), and normalized shear modulus ($G_{eff}/G_0$). Note that $E_0$ and $G_0$ stand for the Young's modulus and shear modulus of the base material (see Supplementary Note 5 for more details). The results are first discussed generally and then for each unit cell category defined in the Methods section: Category I ($\theta_{min}<\theta\leq 90.0^{o}$), Category II ($90.0^{o}<\theta\leq 135.0^{o}$), and Category III ($135.0^{o}<\theta<\theta_{max}$), comprising 17163, 18173, and 9501 data points, respectively.

**Poisson's ratio**. The Poisson's ratio of our geometrically symmetric meta-biomaterials can be continuously tuned from strongly auxetic ($\upsilon=-0.74$) to modestly positive values ($\upsilon=0.33$) based on the $\theta$ and $L/H$, covering an unusually wide spectrum for 3D architected materials. Auxetic behavior was predominantly observed at small strut angles ($\theta<\sim 70^{o}$), particularly when $L/H$ was large. Interestingly, this transition in the sign of Poisson's ratio occurs at significantly smaller $\theta$ values than in conventional 1D or quasi-2D metamaterials (typically at $\theta=90^{o}$[32]), due to the additional geometric constraints introduced by full 3D symmetry.

The effect of $\theta$ on Poisson's ratio depended strongly on $L/H$. At small $L/H$ (<0.14), $\upsilon$ remains nearly constant and close to zero regardless of $\theta$, due to the compact geometry of the unit cells, which behave like rigid inclusions in an effectively cubic framework (Fig. 1i and Supplementary Fig. 3a). In this regime, lateral deformation was limited. At intermediate $L/H$ values ($0.14<L/H<0.48$), $\upsilon$ exhibited a non-monotonic trend, meaning that it decreased in Category I, increased in Category II, and decreased again in Category III (Supplementary Fig. 3a). For larger $L/H$ (> 0.48), typical of Category I, $\upsilon$ decreased with $\theta$. Moreover, while $\upsilon$ increased with $L/H$ in Categories I and II, the opposite trend was observed in Category III, where higher $L/H$ led to more negative $\upsilon$ (i.e., enhanced auxeticity) (Supplementary Fig. 3b). Across the three categories, $\upsilon$ varied within the following ranges: Category I: [-0.74, 0.25], Category II: [0.02, 0.33], and Category III: [0, 0.33].

**Normalized effective elastic modulus**. The distribution of $E_{eff}/E_0$ indicated that the maximum elastic modulus occurred at moderate $L/H$ values ($0.10<L/H<0.35$) in Categories I and II for $\theta>90°$ (Fig. 2a). As $\theta$ increased within this $L/H$ range, $E_{eff}/E_0$ also increased, peaking at $\theta\approx 135°$. Beyond this point (i.e., in Category III), further increases in $\theta$ reduced $E_{eff}/E_0$ (Supplementary Fig. 3a). Moreover, increasing $L/H$ generally reduced $E_{eff}/E_0$ (Supplementary Fig. 3b).

The heatmap in Fig. 2a shows that the number of low-modulus designs (e.g., $E_{eff}/E_0\approx 0.002$) far exceeds that of high-stiffness designs ($E_{eff}/E_0\approx 0.008$). Across all categories, $E_{eff}/E_0$ ranged within the following intervals: Category I: $3.00\times10^{-6}$–$8.40\times10^{-3}$ ($9.13\times10^{-4}\pm1.20\times10^{-3}$), Category II: $3.58\times10^{-6}$–$9.70\times10^{-3}$ ($2.20\times10^{-3}\pm2.20\times10^{-3}$), and Category III: $1.35\times10^{-5}$–$1.00\times10^{-2}$ ($2.50\times10^{-3}\pm2.40\times10^{-3}$). The maximum and minimum $E_{eff}/E_0$ were observed in unit cells from Categories III (i.e., $\theta=150.8^{o}$, $L=65.24/300$ and $d=30.0/300$) and I (i.e., $\theta=80.95^{o}$, $L=144.45/300$ and $d=8.0/300$), respectively (Fig. 2c–i). This trend aligns with established behavior as auxetic architectures (Category I) tend to exhibit lower stiffness, while non-auxetic configurations (Categories II and III) yield higher elastic moduli[33].

**Normalized effective shear modulus.** $G_{eff}/G_0$ showed a normal-like distribution, peaking at $\theta\approx 126.8°$ and $L/H\approx 0.32$ (Supplementary Fig. 3a–c). In Categories I and II, $G_{eff}/G_0$ increased with $\theta$ up to ~126.8°, after which it decreased, particularly in Category III. The population of high-shear-modulus designs was smaller than that of low-shear-modulus ones (Fig. 2a). Designs with very small or large $L/H$ generally exhibited lower $G_{eff}/G_0$ values (Supplementary Fig. 3a, b).

The ranges of $G_{eff}/G_0$ for Categories I, II, and III were $6.44\times10^{-7}$–$2.00\times10^{-3}$ ($1.31\times10^{-4}\pm2.2\times10^{-4}$), $7.1\times10^{-7}$–$9.6\tilde{n}10^{-3}$($4.4\times10^{-4}\pm8.93\times10^{-4}$), and $7.54\times10^{-7}$–$5.8\tilde{n}10^{-3}$ ($2.4\times10^{-4}\pm4.7\times10^{-4}$), respectively. The maximum and minimum of $G_{eff}/G_0$ belong to metamaterials in Categories I (i.e., $\theta=47.95^{o}$, $L=179.7/300$, and $d=8.0/300$), and II (i.e., $\theta=126.8^{o}$, $L=95.2/300$, and $d=30/300$) (Fig. 2c-ii).

**Mechanical anisotropy (Zener ratio)**. The Zener ratio followed a similar distribution to $G_{eff}/G_0$, with a maximum occurring at $\theta\approx 129.3°$ and $L/H\approx 0.34$ (Fig. 2a and Supplementary Fig. 3a–c). Thus, structures in the range $\theta$ = [126°, 129°] and $L/H\approx 0.34$ exhibit both high shear modulus and high anisotropy. The range for $A$ was: Category I: $8.24\times10^{-4}$ – 1.16 ($0.21\pm0.29$), Category II: $8.03\times10^{-4}$ – 1.87($0.33\pm0.47$), and Category III: $8.40\times10^{-4}$ – 0.69 ($0.07\pm0.09$).

https://doi.org/10.1038/s41467-026-77121-y

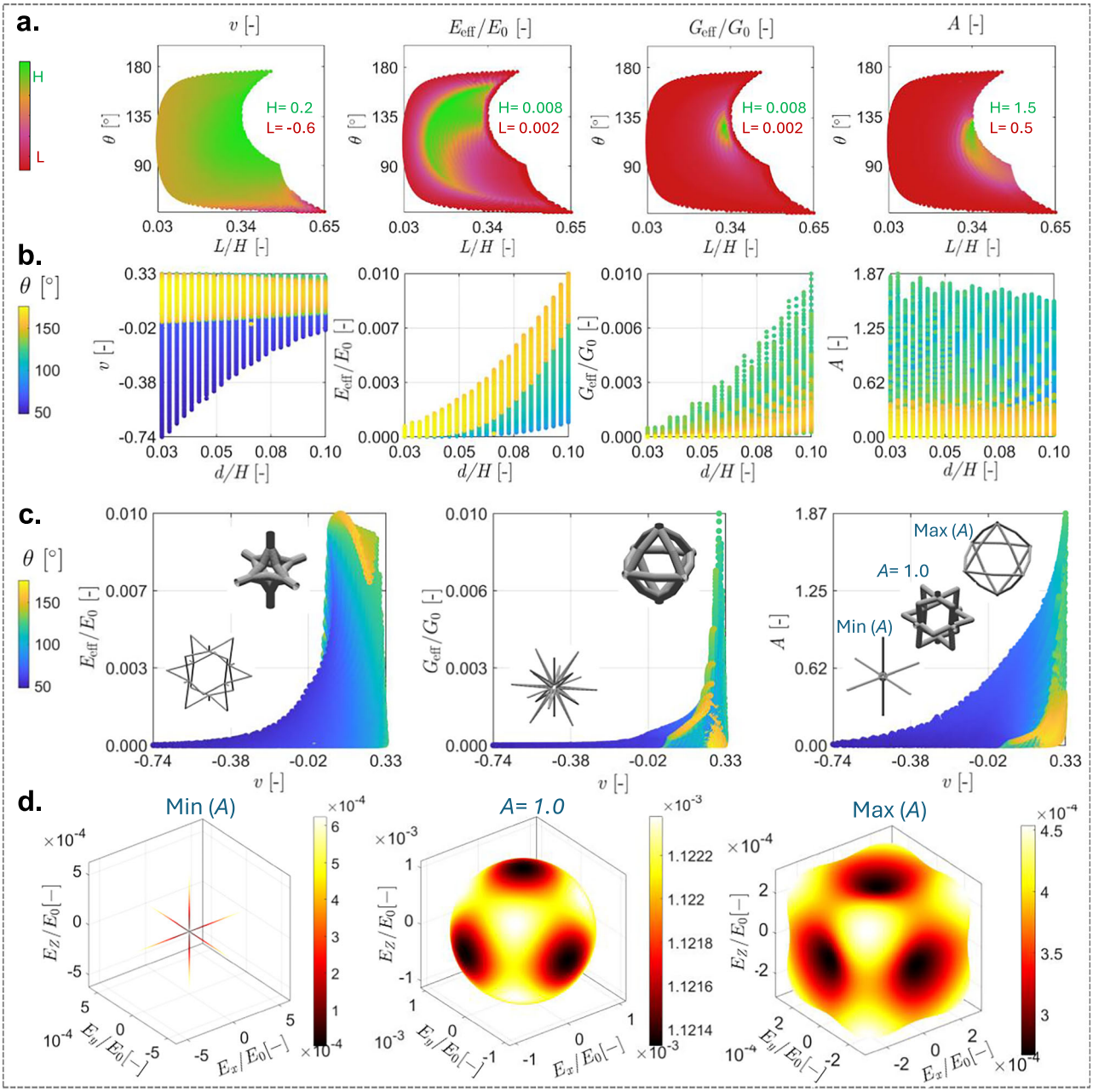



**Fig. 2 | The mechanical properties of the meta-biomaterials. a** The 2D heat map showing the effect of the input parameters $\theta$ and $L/H$ on the mechanical properties ($\upsilon$, $E_{eff}/E_0$, $G_{eff}/G_0$, and $A$). Color bar indicates the maximum ($H$) and minimum ($L$) of each property. **b** The effects of the strut diameter ($d$) on $\upsilon$, $E_{eff}/E_0$, $G_{eff}/G_0$ and $A$. The color bar corresponds to $\theta$ values. **c** The distribution of the elastic properties, including $E_{eff}/E_0$, $G_{eff}/G_0$, and $A$ as a function of Poisson's ratio ($\upsilon$). The voxelized unit cells at the top and bottom of the $E_{eff}/E_0$ and $G_{eff}/G_0$ subplots, respectively, represent the configurations corresponding to the maximal and minimal values of $E_{eff}/E_0$ and $G_{eff}/G_0$. Similarly, the voxelized unit cells at the top, middle and bottom of the $A$ subplot correspond to the maximal, unity, and minimal values of $A$. **d** The stiffness maps of unit cells with minimal ($A_{min} = 8.02 \times 10^{-4}$, left), unity ($A = 1.00$, middle) and maximal Zener ratios ($A_{max} = 1.87$, right). The unit cells corresponding to the minimal, unity, and maximal Zener ratios are respectively represented by $\theta = 120.95^o$, $L = 10.2/300$, and $d = 8.0/300$, $\theta = 84.81^o$, $L = 124.7/300$ and $d = 30.0/300$ and $\theta = 129.29^o$, $L = 102.4/300$, and $d = 9.0/300$. Source data are provided as a Source data file.

The broad distribution in Category II, where the standard deviation exceeds the mean, suggests a wider design space and higher sensitivity to input parameters. Although some designs exhibited $A > 1$, most values remained below unity. Meta-biomaterials with near-isotropic behavior ($A \approx 1$) were mostly in Category II, with positive Poisson's ratios.

**Effect of strut diameter ($d$).** Besides $\theta$ and $L$, the strut diameter significantly influenced all mechanical properties (Fig. 2b). Varying $d$ from 8.0/300 to 30.0/300 led to non-linear changes in $\upsilon$, $E_{eff}/E_0$, $G_{eff}/G_0$, and $A$. Notably, in Category I, increasing $d$ caused $\upsilon$ to become less negative, and eventually positive (i.e., $d > 30.0/300$). This transition was nonlinear and could be counterbalanced by adjusting $\theta$ and $L$. Increasing $d$ consistently enhanced both $E_{eff}/E_0$ and, $G_{eff}/G_0$ but had minimal effect on $A$, rendering $d$ as a less influential parameter in controlling anisotropy.

**Interdependencies and trade-offs.** To further understand the trade-offs, we analyzed the correlation between Poisson's ratio and other mechanical properties (Fig. 2c). For Category I, achieving higher $\upsilon$

https://doi.org/10.1038/s41467-026-77121-y

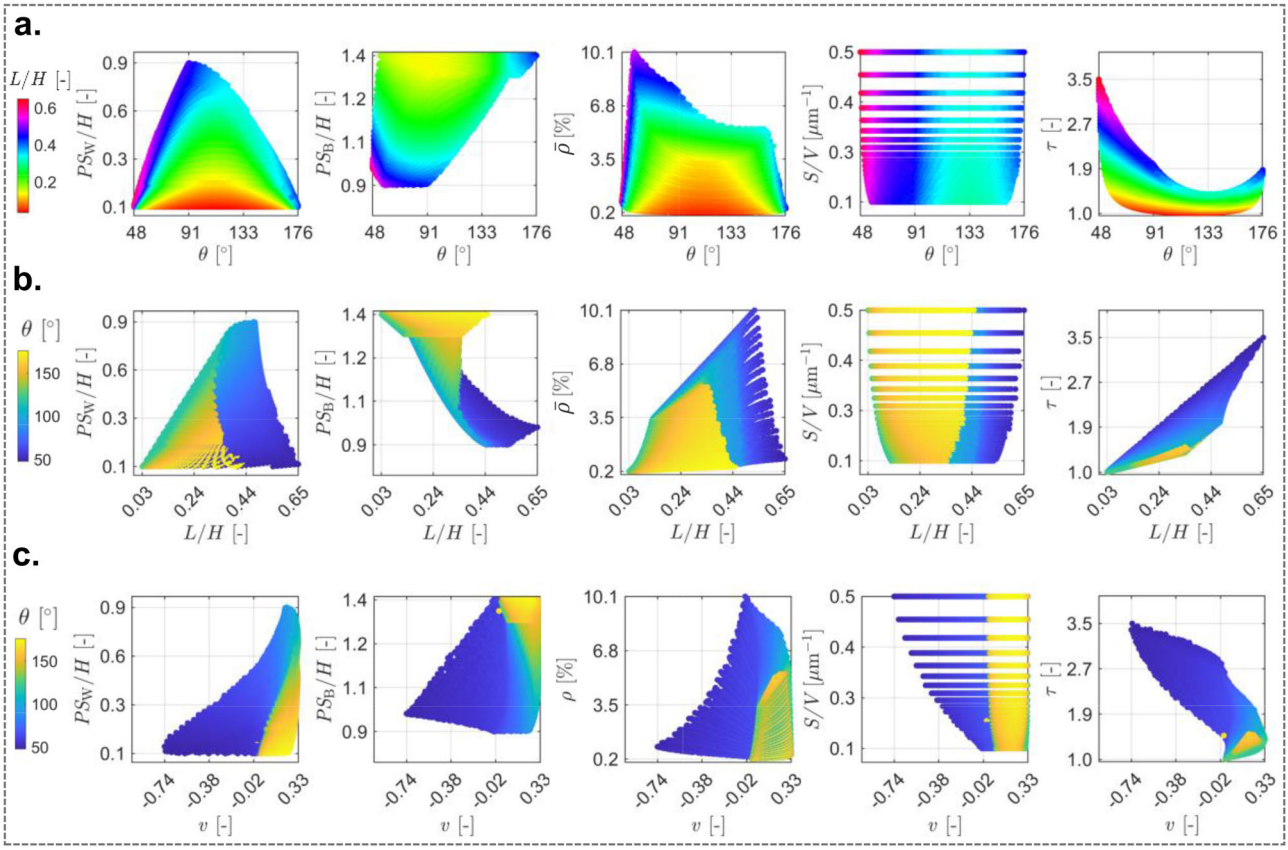



**Fig. 3 | The morphometric properties of the meta-biomaterials. a** The 2D distributions of $PS_W$, $PS_B$, $\bar{\rho}$, $S/V$ and $\tau$ as a function of $\theta$, with the color bar indicating variations of $L/H$. The lower and upper bounds of $L/H$ (corresponding to the purple and red color bars, respectively) exhibit the minimum variation in the morphometric properties as a function of $\theta$. **b** The 2D distributions of $PS_W$, $PS_B$, $\bar{\rho}$, $S/V$ and $\tau$ as a function of $L/H$. The color bar indicates the variation of $\theta$. **c** The evaluation of $PS_W$, $PS_B$, $\bar{\rho}$, $S/V$ and $\tau$ in terms of $\upsilon$, where the color bar indicates the changes in $\theta$. These graphs illustrate the correlations between the morphometric properties and Poisson's ratio, enabling exploration of the meta-biomaterial design space. Source data are provided as a Source data file.

typically required sacrificing $E_{eff}/E_0$, narrowing the design space for stiff auxetic materials[34,35]. In contrast, meta-biomaterials from Category III exhibited the highest $E_{eff}/E_0$ but $\upsilon$ values closer to zero. Interestingly, some designs from different categories (e.g., I and III) had similar $E_{eff}/E_0$ values, suggesting that different microarchitectures can yield the same effective elastic moduli.

Similarly, $G_{eff}/G_0$ displayed a tighter distribution and was highest in designs with positive $\upsilon$ (Categories II and III), contrasting the trend in pentamode metamaterials[14]. The maximum $G_{eff}/G_0$ occurred at maximum $\upsilon$, while maximum $E_{eff}/E_0$ corresponded to $\upsilon \approx 0$. This shows that high elastic and high shear modulus rarely co-occur in the same design.

**Correlation and isotropy.** A clear linear correlation between $E_{eff}/E_0$ and $G_{eff}/G_0$ was observed only in meta-biomaterials with near-isotropic behavior ($0.95 < A < 1.05$), consistent with classical isotropic materials (Supplementary Fig. 3d). However, this linearity was restricted to designs with positive Poisson's ratios.

The Zener ratio provided the broadest design flexibility, especially in the auxetic regime. Designs with high $A$ (> 1.5) were concentrated in Category II ($\theta = 108^\circ - 131^\circ$), and the highest $A$ coincided with the highest $\upsilon$. We identified designs with minimum ($A = 8.02 \times 10^{-4}$), unity ($A$ = 1.00), and maximum ($A$ = 1.87) anisotropy in Categories II (i.e., $\theta = 120.95^o$, $L = 10.2/300$ and $d = 8.0/300$), I (i.e., $\theta = 84.81^o$, $L = 124.7/300$ and $d = 30.0/300$), and II (i.e., $\theta = 129.29^o$, $L = 102.4/300$ and $d = 9.0/300$), respectively (Fig. 2c).

Stiffness maps of these representative designs (Fig. 2d) showed that structures with $A$ <1.00 maintained equal elastic modulus along $x$, $y$, and $z$ due to symmetry, yet exhibited anisotropy in off-axis directions (e.g., 45°). Designs with $A \approx 1$ (mostly $\upsilon = 0.25 \pm 0.03$) were effectively isotropic.

Overall, a sensitivity analysis was performed to quantify the dependence of each meta-biomaterial property on the geometric input parameters ($\theta$, $L/H$, and $d/H$, Supplementary Fig. 3e). This sensitivity analysis showed that Poisson's ratio was most sensitive to variations in the strut angle, whereas the effective shear modulus showed the lowest sensitivity to changes in strut length.

## Morphometric properties of the meta-biomaterials

We quantified the morphometric properties of the meta-biomaterials, including pore size within the unit cell ($PS_W$), pore size between adjacent unit cells ($PS_B$), relative mass density, surface-to-volume ratio ($S/V$) and tortuosity (see Section Materials and Methods for their definitions), across the full range of geometric parameters (i.e., $\theta$, $L$ and $d$), using the derived geometrical relationships (Table 1) and the voxelization-based analysis. The morphometric results are reported as 2D distributions with respect to the input parameters (Fig. 3a, b and Supplementary Fig. 3f), as distributions with respect to Poisson's ratio (Fig. 3c), and as a 3D representation of the design space (Supplementary Fig. 3g).

The variation of $PS_W$ with $\theta$ showed a non-monotonic trend. $PS_W$ increased with $\theta$ up to $120.0^o$, and then decreased as $\theta$ approached its upper bound. Importantly, this behavior depended on $L/H$. For small strut lengths (i.e., $L/H < 0.1$), $PS_W$ was nearly independent of $\theta$, because the unit cell was too compact to substantially alter the pore geometry (Fig. 3a and Supplementary Fig. 3f). For intermediate strut lengths ($0.1 < L/H < 0.4$), the $PS_W$ relationship became approximately

symmetric, indicating that similar $PS_W$ values can be achieved using distinct microarchitectures (notably, from Categories I and III). For larger strut lengths (i.e., $L/H > 0.4$), which occur in Category I, further increasing $L/H$ reduced $PS_W$ (Fig. 3b). In general, $PS_W/H$ ranged from 0.05 to 0.92 ($0.34 \pm 0.18$), 0.05 to 0.93 ($0.44 \pm 0.20$), and 0.05 to 0.64 ($0.25 \pm 0.12$) in Categories I, II, and III, respectively.

When examined against Poisson's ratio, $PS_W$ did not exhibit a consistent global trend (Fig. 3c). Within Category I, however, sharper strut angles corresponded to smaller (tighter) $PS_W$ values, consistent with Supplementary Equation (5). This behavior mirrors the narrowing observed in the elastic and shear modulus distributions corresponding to more negative Poisson's ratios (Fig. 2a). Consequently, achieving auxetic meta-biomaterials with relatively higher Poisson's ratios (within the auxetic regime) constrains the accessible $PS_W$ design space, requiring smaller $\theta$ values.

In contrast to $PS_W$, $PS_B$ varied positively with respect to $\theta$ and $L$ (Fig. 3a). In Category III, $PS_B$ approached a plateau at $\theta \approx 155.0^o$ and remained nearly unchanged with further increase in $\theta$. This plateau corresponds to the geometric upper bound where $PS_B$ equals the face diagonal of the cubic domain, $\sqrt{2}H - d$ (Fig. 1e). Small variations within this plateau region were primarily due to differences in strut diameter. The $L/H$ values associated with this plateau were approximately 0.30 to 0.45. As expected, for very small $L/H$ values, $PS_B$ was nearly independent of $\theta$ because strut length contributes minimally to the overall architecture (Supplementary Fig. 3f). Across the design space, increasing $L/H$ decreased $PS_B$ (Fig. 3b). Generally, $PS_B/H$ ranged from 0.91 to 1.39 ($1.11 \pm 0.14$), 0.92 to 1.39 ($1.23 \pm 0.12$) and 1.18 to 1.39 ($1.35 \pm 0.04$) in Categories I, II and III, respectively. These ranges indicate that Category III exhibits relatively weak sensitivity of $PS_B$ to the input parameters resulting in a narrower $PS_B$ design space as compared to the other categories. Similar to $PS_W$, $PS_B$ displayed a largely irregular distribution with respect to $\upsilon$ (Fig. 3c), which can further complicate systematic property decoupling.

Relative mass density ($\bar{\rho}$), or porosity ($100 - \bar{\rho}[\%]$), showed strong dependence on $L/H$ and reached its highest values in Category I for $L/H > 0.35$ (Fig. 3a, Supplementary Fig. 3f and Supplementary Fig. 3e for all data), consistent with previous reports[1]. For very small $L/H$, the unit cells contribute little to the global solid volume fraction, and the dependence of relative mass density on $\theta$ becomes negligible (Fig. 3c). At moderate $L/H$ values ($L/H$ <0.4), the $\rho - \theta$ relationship was approximately symmetric, implying that microarchitectures from Category I can match the relative mass density of designs from Category III (Fig. 3a). The $\theta$ at which relative mass density peaked depended on $L/H$ and spanned a broad interval. Overall, increasing $L/H$ increased relative mass density, as expected from the increased material volume required for longer struts. Relative mass density ranged from 0.21 to 10.13 ($2.64 \pm 1.98$), 0.20 to 7.79 ($2.01 \pm 1.45$), and 0.20 to 5.41 ($1.64 \pm 1.21$) for Categories I, II, and III, respectively. When plotted against Poisson's ratio, the relative mass density exhibited an irregular pattern (Fig. 3c), highlighting the intrinsic coupling that makes optimization and decoupling non-trivial.

In contrast to the above properties, $S/V$ was largely independent of $\theta$ and $L$ (Fig. 3a, b and Supplementary Fig. 3e, f). This behavior can be explained by Supplementary Equation (22), which indicates that $S/V$ depends primarily on strut diameter. Accordingly, in our designs, $S/V$ ranged from 0.13 to 0.5 as $d/H$ increased from 8.0/300 to 30.0/300. Moreover, the $S/V - \upsilon$ distribution suggests that increasing $S/V$ expands the accessible range of Poisson's ratio, particularly in the auxetic region, because higher $S/V$ corresponds to smaller strut diameters (Fig. 3c).

Finally, tortuosity ($\tau$) followed an ordered dependence on $\theta$ and $L/H$ (Fig. 3a). Category I exhibited higher tortuosity, whereas Categories II and III, particularly Category II, showed lower values. This trend is explained by the smaller vertical height $h$ in Category II (Supplementary Fig. 1a), which yields a smaller shortest flow path length ($L_{short}$) and therefore lower tortuosity (explained by Supplementary Equation (23)). In Categories I and II, increasing $\theta$ reduced tortuosity (most strongly in Category I), consistent with a smoother transport pathway or reduced $L_{short}$ as $\theta$ approaches 135° (Supplementary Equation (24)). Increasing $L/H$ increased $L_{short}$ and therefore increased tortuosity across all categories. When analyzed against Poisson's ratio, designs with positive $\upsilon$ (Categories II and III) occupied a narrower tortuosity range than auxetic designs, reducing the feasible design space for $\tau$-based decoupling (Fig. 3c). Tortuosity ranged from 1.08 to 3.50 ($1.91 \pm 0.43$), 1.04 to 1.95 ($1.34 \pm 0.17$), and 1.05 to 1.84 ($1.32 \pm 0.13$) in Categories I, II, and III, respectively.

## Decoupling the properties of the meta-biomaterials

The objective of this section was to identify optimized pairs of meta-biomaterials that exhibit the maximal contrast in a single target property (e.g., Poisson's ratio) while maintaining minimal deviations in all remaining mechanical, and morphometric properties (i.e., decoupled property). In the specific case of decoupling Poisson's ratio, we aimed to identify pairs in which one meta-biomaterial exhibits a negative Poisson's ratio (auxetic behavior) and the other a positive Poisson's ratio, while the remaining properties remain as similar as possible. This strategy provides a systematic and versatile framework for disentangling complex interdependencies among multiple properties in architected meta-biomaterials, thereby enabling targeted optimization of individual parameters. It should be noted that the decoupling procedure was performed following the validation of the numerical results (Table 2).

Pairs of designs satisfying the maximum variation criteria defined by Eqs. (5 and 6) were considered as optimal. Specifically, Eq. (7) was used for Poisson's ratio and Eq. (8) for other properties, such as pore size. The optimization outcomes for six different variation thresholds ($\min Var$) are summarized in Fig. 4a, together with the corresponding deviations of each property ($D_x$). For all properties except Poisson's ratio, deviations were quantified using Eq. (5). For the Poisson's ratio, we plotted the deviation as $\left|\upsilon_i - \upsilon_j\right|$.

First, with respect to connectivity, all generated meta-biomaterials, regardless of $\theta$ and $L$, exhibited identical connectivity. This uniformity arises from the fixed nodal arrangement and element count of the unit cells (Fig. 1). Given the local connectivity of two for the marginal nodes (P1, P5, P8, P13, P16, and P19 in Fig. 1g), application of Supplementary Equation (20) yields a global connectivity of 2.42 for all designs.

Analysis of Fig. 4a indicates that pore size (represented by $PS_B$ in the optimization framework) and surface-to-volume ratio are the most difficult properties to decouple from the remaining descriptors, as their deviations remain large even at low variation thresholds (i.e., $D >$ $\min Var$). Other properties that also exhibit limited decoupling potential include tortuosity (e.g., $D_{\tau,\,\max} \approx 34\%$ at $\min Var = 20\%$), effective elastic modulus ($D_{E,\,\max} \approx 37\%$ at $\min Var = 20\%$), shear modulus ($D_{G,\,\max} \approx 39\%$ at $\min Var = 20\%$), and degree of anisotropy ($D_{A,\,\max} \approx 40\%$ at $\min Var = 20\%$). These results indicate that, depending on the tolerated variation level and acceptable error in preserving other properties, shear modulus and anisotropy can be regarded as only partially decoupled.

In contrast, Poisson's ratio and relative mass density emerged as the most effectively decoupled properties in this study. As shown in Fig. 4a, Poisson's ratio and relative mass density reached deviations of $D_\upsilon \approx 174\%$ and $D_{\bar{\rho}} \approx 50\%$ at $\min Var = 20\%$, respectively. This finding was further supported by Pareto-front analysis, which quantified the trade-off between maximizing variations in Poisson's ratio or relative mass density while minimizing deviations in the remaining properties (Fig. 4b). The Pareto fronts demonstrated that both properties can be tuned over a relatively broad range while maintaining limited changes in the other effective properties. Beyond the Pareto-optimal regions, however, larger variations in the target properties were associated with

**Table 2 | The numerical and experimental results of the validation meta-biomaterials (samples 1-5)**

| Meta-biomaterial | | Homogenization method | | | 3D solid elements | Experiment | | | SolidWorks |
|---|---|---|---|---|---|---|---|---|---|
| $\theta$[°], $L$[×1/300] $d$[×1/300] | Unit cell | $E_{eff}/E_0$ [$\times 10^{-4}$] | υ [–] | ρ [%] | $E_{eff}/E_0$ [$\times 10^{-4}$] | υ [–] | $E_{eff}/E_0$ [$\times 10^{-4}$] | υ [–] | ρ [%] |
| 60, 110, 20 **(Sample 1)** |  | 8.532 | -0.03 | 3.48 | 8.320 | -0.06 | 8.333 | 0.051 | 3.46 |
| 60, 140, 14 **(Sample 2)** |  | 0.780 | -0.19 | 2.14 | 0.800 | -0.22 | 1.108 | -0.177 | 2.12 |
| 90, 100, 14 **(Sample 3)** |  | 0.970 | 0.24 | 1.50 | 0.960 | 0.24 | 0.831 | 0.152 | 1.48 |
| 120, 90, 14 **(Sample 4)** |  | 4.4800 | 0.32 | 1.27 | 4.640 | 0.30 | 3.402 | 0.289 | 1.26 |
| 150, 100, 14 **(Sample 5)** |  | 4.524 | 0.32 | 1.33 | 4.720 | 0.30 | 3.462 | 0.347 | 1.31 |

Note that the experimental results are reported as mean values, considering sample size $n = 3$. Source data are provided as a Source Data file and the Supplementary Data files (Supplementary Videos#6–10)

substantially greater deviations in the remaining properties, highlighting the intrinsic coupling between these properties. Accordingly, Poisson's ratio and relative mass density were successfully decoupled from the remaining properties with average deviations of other properties below 15% (Table 3, both Pairs I and II), and 8.20% (Table 4), respectively.

For Poisson's ratio, two optimized pairs (Pairs #I and #II) were identified. Pair #I was selected for experimental validation due to its relatively larger strut diameter. The corresponding unit cells, labeled Unit cell P#I1 and P#I2, as well as those associated with the decoupled relative mass density (R#I and R#II), are shown in Fig. 4c and Supplementary Videos 2–3 and 4–5, respectively. The Poisson's ratio-isolated designs both belong to Category I, with $\upsilon = -0.11$ for the auxetic design and $\upsilon = 0.09$ for the non-auxetic design (from Pair #I). In contrast, the relative mass density-isolated designs belong to Category I ($\theta = 86.81°$, $L/H = 132.73/300$, $d/H = 30.0/300$, $\bar{\rho} = 8.07\%$) and Category II ($\theta = 97.03°$, $L/H = 97.54/300$, $d/H = 24.0/300$, $\bar{\rho} = 4.04\%$).

To assess the mechanical anisotropy of the decoupled designs, stiffness maps were constructed for all optimized pairs (Fig. 4c, d). The stiffness maps of the Poisson's ratio-isolated designs (Unit cell P#I1 and P#I2) showed cubic symmetry, with normalized elastic and shear moduli of $E_{eff}/E_0 = 2.059 \times 10^{-4}$ and $G_{eff}/G_0 = 4.643 \times 10^{-6}$, respectively (Table 3, Unit cell P#I1). Despite this symmetry, the narrow stiffness surfaces indicate extreme mechanical anisotropy, meaning that these designs exhibit substantially different mechanical responses along non-orthogonal directions ($A = 0.014$ and 0.017 for Unit cell P#I1 and P#I2, respectively). All mechanical and morphometric properties of P#I1 and P#I2 are reported in Table 3. While these two designs show very similar pore sizes (6.39% deviation), differences in the remaining properties remain below 20%.

In contrast, the relative mass density-isolated designs (R#I and R#II) exhibit high mechanical isotropy, characterized by a Zener ratio of approximately 0.92 (Fig. 4d). Unlike Poisson's ratio-isolated designs, R#I and R#II display similar mechanical behavior not only along the three orthogonal axes but also along non-orthogonal directions.

We also reported the tortuosity of the optimized meta-biomaterials computed using an analytical expression (Supplementary Eq. (24)), and a voxel-based 3D analysis using a customized ImageJ plugin[36]. The distribution and mean values of tortuosity are shown in Fig. 5a. For the Poisson's ratio-isolated designs, Supplementary Eq. (24) predicted tortuosity values of 1.95 (unit cell P#I1) and 1.58 (unit cell P#I2), compared with 1.77 and 1.43 obtained from the voxel-based model, respectively, indicating good agreement. For the relative mass density-isolated designs, Supplementary Equation (24) yielded values of 1.58 (R#I) and 1.94 (R#II), whereas the voxel-based analysis yielded values of 1.47 and 1.20. The larger discrepancy for R#II is attributed to its larger strut diameter, which is not explicitly accounted for in Supplementary Eq. (24). Nevertheless, this comparison suggests that the analytical tortuosity model is valid.

To further illustrate the tortuosity behavior of the optimized meta-biomaterials, the distributions of Euclidean path length ($L_e$) vs. straight-line distance ($L_g$) are depicted in Fig. 5a. These distributions exhibit larger fluctuations for the Poisson's ratio-isolated design (P#I2) compared with the relative mass density-isolated design (R#I), reflecting the sharper strut angles in the former.

Finally, permeability values calculated *via* FE modeling (Tables 3 and 4; Supplementary Fig. 4e, f) exhibited substantial decoupling relative to other properties, with deviations of 20.78% for the Poisson's ratio-isolated designs (P#I1 and P#I2) and 71.29% for the relative mass density-isolated pair (R#I and R#II). The associated pressure fields and velocity contours are present in Supplementary Fig. 4e, f. The similarity between permeability trends and those of tortuosity and relative mass density reflects the intrinsic coupling

https://doi.org/10.1038/s41467-026-77121-y

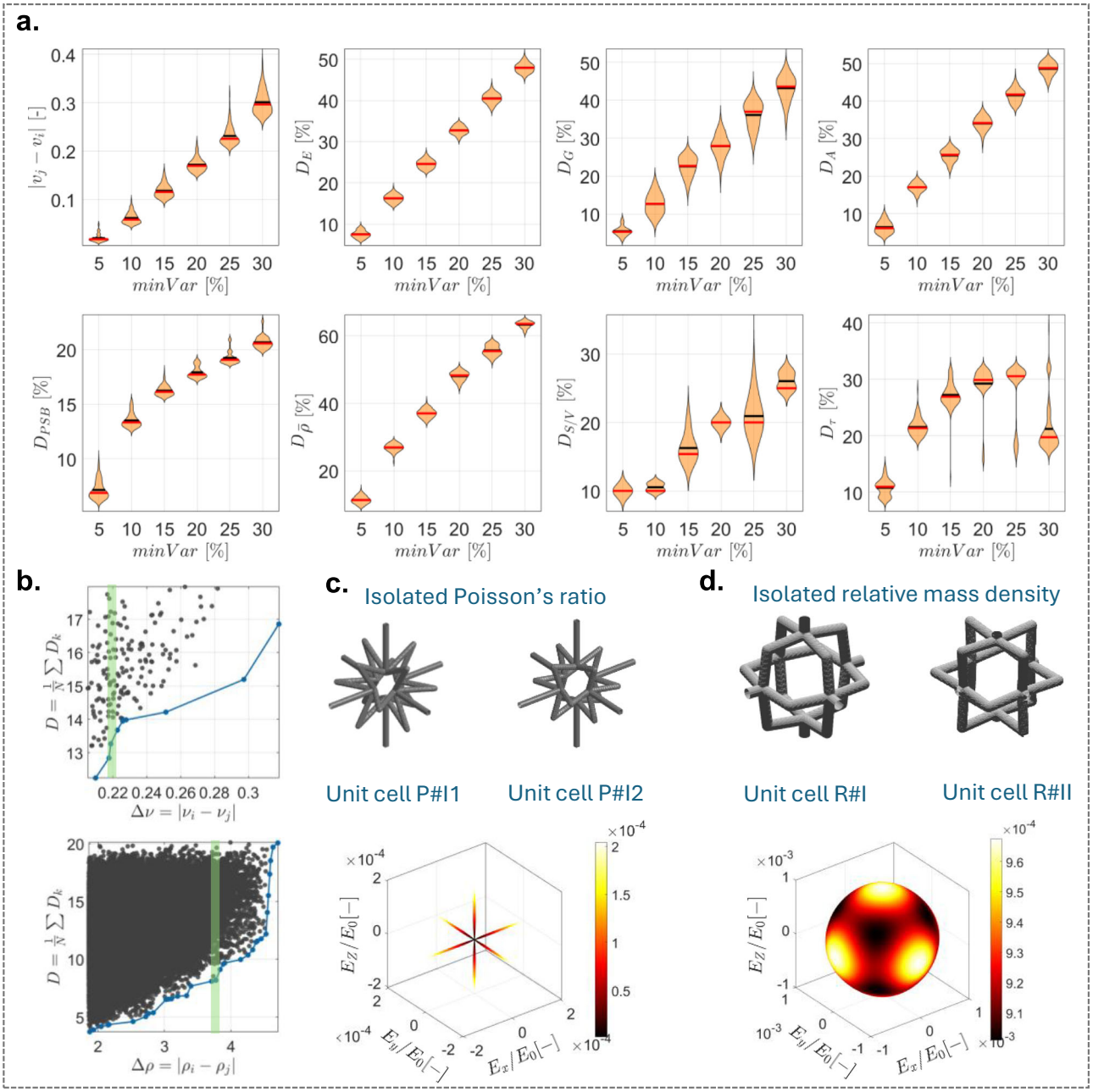



**Fig. 4 | The results of the multi-objective optimization for isolating individual parameters. a** Violin plots depicting the deviation ($D_x$) of the optimized meta-biomaterials isolated at six variation thresholds (min $Var$) 5%, 10%, 15%, 20%, 25% and 30%. Note that for the case of the Poisson's ratio isolation, the absolute differences between paired Poisson's ratios have been reported instead of the deviation. The black and red solid lines indicate the Mean and Median values, respectively. **b** Pareto-front plots illustrating the optimal trade-off between maximizing the contrast in the target property (i.e., Poisson's ratio (top) or relative mass density (bottom)), and minimizing the total deviation of the remaining properties. The blue curve represents the Pareto-optimal front, while the green shaded region indicates the selected design space used for the final optimized solutions. **c** The configuration of the unit cells of the decoupled meta-biomaterials in terms of Poisson's ratio, accompanied by their respective stiffness map. Note that we reported the stiffness of the unit cell P#I1 here. **d** The configuration of the unit cells R#I and R#II, with isolated relative mass density, along with their corresponding stiffness map.

among these properties, which often follow nonlinear relationships[37]. Consequently, controlling one of these parameters can partially influence the others. In future optimization studies, permeability could be explicitly incorporated as an additional objective to further decouple it from relative mass density.

### 3D printing and mechanical characterization of the meta-biomaterials

To experimentally validate the predictions of our computational framework, we 3D-printed five representative meta-biomaterials and characterized their effective elastic moduli and Poisson's ratios under uniaxial compression (Table 2).

The selected meta-biomaterials span different geometric categories and input parameter combinations (Table 2) and were fabricated using an inkjet-based, UV-cured PolyJet 3D printing process (Fig. 5b). The compression behavior of the 3D printed specimens was evaluated under quasi-static uniaxial loading at a displacement rate of 3 mm min$^{-1}$. The resulting stress-strain responses are shown in Fig. 5c, with quantitative values summarized in Table 2 and corresponding deformation videos provided in Supplementary Videos 6–10. The

**Table 3 | The mechanical, morphometric and mass-transport properties of the meta-biomaterials with isolated Poisson's ratio**

| Parameter | Pair I | | | Pair II | | |
|---|---|---|---|---|---|---|
| | Unit cell P#I1 | Unit cell P#I2 | Deviation [%] | Unit cell P#II1 | Unit cell P#II2 | Deviation [%] |
| $\theta$ [°] | 59.31 | 71.31 | - | 57.95 | 72.95 | |
| $L/H$[−] | 86.48/300 | 63.71/300 | - | 62.85/300 | 43.10/300 | - |
| $d/H$[−] | 13/300 | 13/300 | - | 8/300 | 8/300 | - |
| $\nu$ [−] | −0.11 | 0.09 | 180.68 | −0.13 | 0.10 | 177.43 |
| $E_{eff}/E_0$[−] | $2.059\times10^{-4}$ | $2.540\times10^{-4}$ | 18.95 | $1.186\times10^{-4}$ | $1.450\times10^{-4}$ | 18.18 |
| $G_{eff}/G_0$[−] | $4.643\times10^{-6}$ | $5.828\times10^{-6}$ | 20.33 | $8.120\times10^{-7}$ | $9.710\times10^{-7}$ | 16.38 |
| $A$ [−] | 0.014 | 0.017 | 20.35 | 0.0041 | 0.0051 | 18.96 |
| $PS_B/H$ [−] | 1.19 | 1.27 | 6.39 | 1.33 | 1.39 | 4.38 |
| $\rho$ [%] | 1.10 | 0.87 | 20.72 | 0.41 | 0.33 | 21.15 |
| $S/V$[$\mu m^{-1}$] | 0.33 | 0.33 | 0 | 0.5 | 0.5 | 0 |
| $\tau$[−] | 1.95 | 1.58 | 18.87 | 1.71 | 1.39 | 18.82 |
| $Z_g$ [−] | 2.42 | 2.42 | 0 | 2.42 | 2.42 | 0 |
| $k$[$m^2$] | $3.85\times10^{-6}$ | $4.86\times10^{-6}$ | 20.78 | $6.68\times10^{-6}$ | $7.65\times10^{-6}$ | 12.68 |
| $D_{avg}$ [%] | - | - | 14.04 | - | - | 12.28 |
| Experiments | | | | | | |
| $\nu$ [−] | -0.103 | 0.074 | 171.84 | - | - | - |
| $E_{eff}/E_0$[−] | $1.987\times10^{-4}$ | $2.459\times10^{-4}$ | 19.21 | - | - | - |
| $k$[$m^2$] | $2.15\times10^{-6}$ | $2.99\times10^{-6}$ | 39.38 | - | - | - |

Two pairs were selected with isolated Poisson's ratio, including $\theta_1 = 59.31°$, $L_1 = 86.48/300$, $d_1 = 13/300$ and $\theta_1 = 71.31°$, $L_1 = 63.71/300$, $d_1 = 13/300$ for the pair I, and $\theta_1 = 57.95°$, $L_1 = 62.85/300$, $d_1 = 8.0/300$ and $\theta_1 = 72.95°$, $L_1 = 43.10/300$, $d_1 = 8.0/300$ for pair II. Note that the experimental results are reported as mean values, considering sample size $n = 3$. Source data are provided as a Source Data file and the Supplementary Data files (Supplementary Videos#11 and 12).

**Table 4 | The mechanical, morphometric and mass-transport properties of the meta-biomaterials with isolated relative mass density (i.e., $\theta_1 = 97.03°$, $L_1 = 97.54/300$, $d_1 = 24.0/300$ and $\theta_2 = 86.81°$, $L_2 = 132.73/300$, $d_1 = 30.0/300$)**

| Parameter | Unit cell R#I | Unit cell R#II | Deviation [%] |
|---|---|---|---|
| $\theta$ [°] | 97.03 | 86.81 | - |
| $L/H$[−] | 97.54/300 | 132.73/300 | - |
| $d/H$[−] | 24/3900 | 30/300 | - |
| $\nu$ [−] | 0.26 | 0.22 | 15.57 |
| $E_{eff}/E_0$[−] | $9.676\times10^{-4}$ | $9.186\times10^{-4}$ | 5.06 |
| $G_{eff}/G_0$[−] | 0.0010 | 0.0010 | 0 |
| $A$ [−] | 0.92 | 0.94 | 2.32 |
| $PS_B/H$ [−] | 1.04 | 0.91 | 4.03 |
| $\rho$ [%] | 4.04 | 8.07 | 49.94 |
| $S/V$[$\mu m^{-1}$] | 0.17 | 0.13 | 20 |
| $\tau$[−] | 1.58 | 1.94 | 18.60 |
| $Z_g$ [−] | 2.42 | 2.42 | 0 |
| $k$[$m^2$] | $1.39\times10^{-6}$ | $3.99\times10^{-7}$ | 71.29 |
| $D_{avg}$[%] | - | - | 8.20 |
| **Experiments** | | | |
| $\nu$ [−] | 0.163 | 0.083 | 49.08 |
| $E_{eff}/E_0$[−] | $7.668\times10^{-4}$ | 0.0016 | 52.08 |
| $k$[$m^2$] | $1.07\times10^{-6}$ | $0.753\times10^{-6}$ | 29.59 |

Note that in the calculation of the average deviation of the properties ($D_{avg}$), permeability has not been considered. Note that the experimental results are reported as mean values. Source data are provided as a Source Data file and the Supplementary Data files (Supplementary Videos#13 and 14).

experimentally measured effective elastic moduli exhibit good agreement with both homogenization-based predictions and 3D solid FE results. In particular, for specimens with relatively thick struts (e.g., sample 1), the experimentally measured modulus closely matches the numerical prediction ($8.333\times10^{-4}$ vs. $8.532\times10^{-4}$). As discussed in the validation section (Supplementary Note 4), the discrepancy between the homogenization method and the 3D solid FEM simulations is negligible, demonstrating the high accuracy of the homogenization approach. Consequently, the remaining differences between experimental and numerical values are most likely attributable to printing imperfections, potential specimens sliding at the loading interfaces, and measurement uncertainties associated with the testing apparatus.

Under uniaxial compression, the meta-biomaterials exhibited different extents of linear elastic behavior, with linear strain ranges of approximately 1.8%, 3.3%, 5.0%, 3.3%, and 3.2% for specimens 1–5, respectively. The smaller linear regime observed for specimen 1 is consistent with its relatively high effective elastic modulus. The linear portions of the stress-strain curves (Fig. 5c) indicate that meta-biomaterials 1, 2, 4, and 5 exhibit comparable elastic moduli. In contrast, meta-biomaterial 3, which consists of cubic unit cells ($\theta = 90°$), displays larger fluctuations in the linear regime (Fig. 5). These fluctuations become more pronounced in the nonlinear deformation regime at higher strains, where densification and structural damage occur. Since the nonlinear response is beyond the scope of the present study, it is not discussed further here.

Poisson's ratios were also experimentally measured for all five meta-biomaterials (Table 2), showing reasonably good agreement with computational predictions. The observed discrepancies between the experimental and numerical results can be attributed to printing imperfections, limitations in numerical modeling resolution (*e.g.*, mesh density and voxelization degree), and the accuracy of the measurement setup. Further improvements in measurement accuracy could be achieved in future work by employing more advanced digital image correlation or image-processing techniques.

In addition to the baseline designs, we fabricated meta-biomaterials corresponding to the optimized, decoupled pairs for Poisson's ratio and relative mass density (Fig. 5d; Supplementary Videos 11–14). For Poisson's ratio, the design from Pair I (Table 3) was selected for fabrication due to its thicker struts as compared to Pair II. The compression responses of the decoupled Poisson's-ratio specimens, measured at a displacement rate of 3 mm $min^{-1}$, are presented in

https://doi.org/10.1038/s41467-026-77121-y

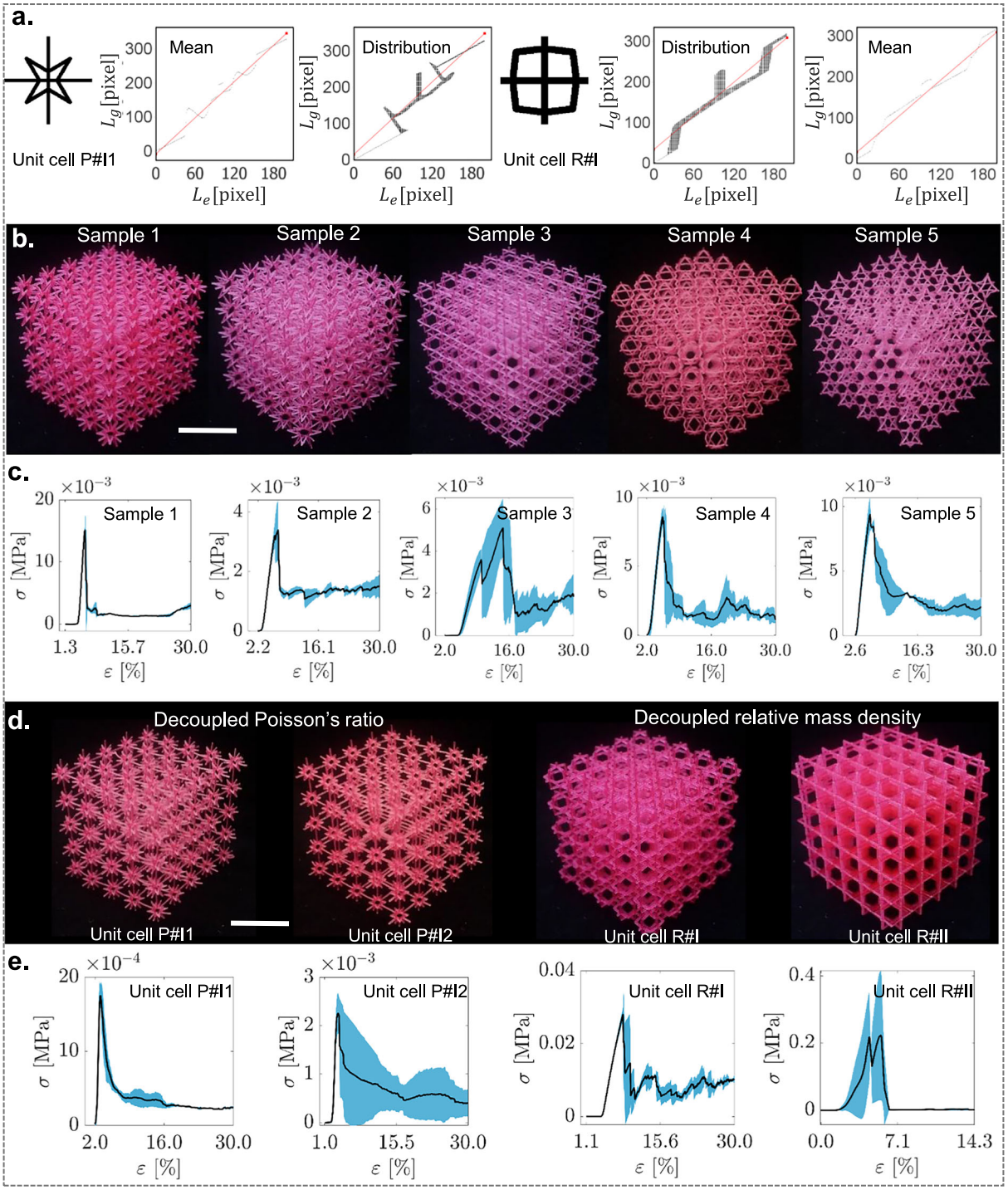



**Fig. 5 | Post-assessment of the optimized meta-biomaterials in terms of mechanical and morphometric properties. a** Tortuosity results for the decoupled meta-biomaterials based on their 3D voxelized unit cells. The correlation between the Euclidean ($L_e$) and straight path lines ($L_g$) in terms of their mean values and distribution within the decoupled meta-biomaterials with respect to Poisson's ratio (unit cell P#I1), and relative mass density (unit cell R#I). The red solid line indicates the best linear fit for the mean and distribution of the lengths. The mechanical characterization of the meta-biomaterials at the macroscale. **b** Optical images of the PolyJet 3D-printed meta-biomaterials mentioned in Table 1 (Samples 1–5) for validating our computational model. The scale bar corresponds to 25 mm. **c** The result of the uniaxial compression test (stress ($\sigma$) vs. strain ($\varepsilon$) plot) of the 3D printed meta-biomaterials under a displacement rate of 3 mm min$^{-1}$. The dark solid line represents the mean, and the blue shadow indicates the upper/lower bounds, considering sample size $n = 3$. **d** Optical images of the PolyJet 3D-printed optimized meta-biomaterials with isolated Poisson's ratios (two on the left) and isolated relative mass density (the other two on the right). The scale bar corresponds to 25 mm. **e** The stress/strain behavior of the decoupled meta-biomaterials under a uniaxial compression test with a 3 mm min$^{-1}$ displacement rate. The black solid line and the blue shadow indicate the mean and the upper/lower bounds, considering sample size $n = 3$. Source data are provided as a Source data file.

Fig. 5e. The experimentally measured effective elastic moduli of these designs agree well with the numerical predictions (Table 3), supporting the validity of the decoupling strategy.

For the relative mass density-isolated designs, unit cell R#II exhibited substantially higher reaction forces than unit cell R1. This behavior arises from the geometry of R#II in which strut overlap occurs at relatively small strains. Consequently, the effective elastic modulus of R#II was evaluated at a small strain level (0.6%). Although the experimentally measured modulus of R#II remains higher than the homogenization-based prediction (0.0016 vs. $9.186 \times 10^{-4}$, corresponding to a 43% difference; Table 4), the agreement for unit cell R#I is considerably better ($9.676 \times 10^{-4}$ versus $7.668 \times 10^{-4}$, corresponding to a 21% difference).

The permeability values predicted for the decoupled meta-biomaterials were also compared with experimental measurements (Tables 3 and 4). Despite the use of a relatively simple gravity-driven experimental setup, the discrepancies between numerical and experimental permeability values remained moderate (44.15%, 38.48%, 23.02%, and 47.01% for unit cells P#I1, P#I2, R#I, and R#II, respectively). Similar to Poisson's ratio measurements, achieving lower discrepancies in permeability will require more precise experimental configurations in future studies.

To demonstrate scalability, we further fabricated meta-biomaterials at the microscale using 2PP, enabling micrometer-scale feature resolution (Supplementary Fig. 5). These included designs with various input parameters, notably a meta-biomaterial with the minimum strut diameter ($d/H = 8.0/300$; Supplementary Figs. 5a-iv and 5a-v), highlighting the manufacturability of the proposed architectures across multiple length scales. A representative compression test of a microscale meta-biomaterial ($\theta = 65.0°$, $L/H = 110.0/300$, $d/H = 20.0/300$) is shown in Supplementary Fig. 5b, together with an optical image of the deformed structure.

It should be noted that further improvements in property decoupling, particularly for challenging descriptors such as tortuosity, could be achieved by introducing hollow or variable-thickness struts instead of solid ones. Hollow architectures would provide additional geometric degrees of freedom to independently tune mechanical and morphometric properties. However, fabricating such structures at the microscale remains challenging, as removing trapped resin from enclosed cavities is highly challenging even with 2PP. An alternative strategy is to adopt stochastic microarchitectures, which offer greater design freedom and may further facilitate property decoupling in future investigations.

Finally, the decoupled meta-biomaterials presented here exhibit ultimate compressive stresses on the order of ~20 kPa (Fig. 5e). This mechanical performance could be enhanced through several routes, including (*i*) employing stiffer base materials such as metals or hybrid polymer-ceramic composites, (*ii*) optimizing printing parameters to increase polymerization or bonding quality, (*iii*) relaxing the degree of decoupling, (*iv*) reducing the number of simultaneously constrained properties, or (*v*) restricting Poisson's ratio to narrower target ranges, depending on the intended application.

## Methods

### Geometrical design of the meta-biomaterials

The detailed derivation of the equations for the geometrical design of our meta-biomaterials is provided in Supplementary Note 1, along with a summary of all the geometrical relationships presented in Table 1. To simplify the derivation of the geometrical equations and the interpretation of results, we categorized our designs into three groups, namely Category I, Category II, and Category III, based on the parameters $\theta$ and $L$ (Fig. 1c). These categories are defined as follows:

Category I: $\theta_{min} < \theta \le 90.0^o$ and $L_{min} < L \le L_{max}$,
Category II: $90.0^o < \theta \le 135.0^o$ and $L_{min} < L \le L_{max}$,
Category III: $135.0^o < \theta < \theta_{max}$ and $L_{min} < L \le L_{max}$,

In our designs, two distinct pore sizes were defined, given that the proposed meta-biomaterials are composed of repetitively arranged monolithic unit cells. The first pore size refers to the internal pore shape within the unit cell, termed as the "pore size within" ($PS_W$, represented by the dark green sphere in Fig. 1h). The second pore size is defined by the voids created between adjacent unit cells, referred to as the "pore size between" ($PS_B$, represented by the light green sphere in Fig. 1h). These pore sizes have direct and explicit relationships with $\theta$ and $L$, the actual form of which depends on the Category. It should be noted that $PS_W < PS_B$ and therefore, in the final optimization step we considered $PS_B$ as representations of pore size.

After extracting all the geometrical correlations for the critical values of the input parameters, we generated a large number of unit cells within the design space defined by our model (*i.e.*, $\theta_{min}$, $\theta_{max}$, $L_{min}$, and $L_{max}$, as shown in Fig. 1k). The generation process is further illustrated in Supplementary Video 1. We solved the geometrical relationships (Supplementary Eqs. (18 and 19)) via *fsolve* function in MATLAB (R2024b, MathWorks, USA) and generated all the designs of the meta-biomaterials in MATLAB.

### Voxelization of the meta-biomaterials

For voxel-based modeling, a single unit cell was considered as the representative volume element and enclosed within a cubic domain of side length $H$, which was normalized to unity ($H = 300/300 = 1$) along the three orthogonal directions ($x$, $y$, and $z$). The unit cell was discretized into an $n \times n \times n$ grid of cubic voxels, where $n$ denotes the number of voxels per direction, resulting in a voxel edge length of $H/n$. The discretized domain was represented as a binary 3D matrix, in which a value of 1 denotes solid material, and 0 denotes void.

A voxel was classified as solid if the minimum distance between its center and any strut axis was smaller than the corresponding strut radius. The voxelization algorithm was adapted from reference[31] but was substantially optimized to improve computational efficiency, achieving at least a tenfold reduction in execution time, particularly for unit cells with low porosity (i.e., larger strut diameters). The principal optimizations included: (*i*) eliminating redundant calculations by using a precomputed logical mask to identify solid voxels, followed by a single update step rather than iterative voxel-strut evaluations; (*ii*) employing vectorized operations instead of nested loops to generate voxel-center coordinates and compute distances simultaneously for all voxels; and (*iii*) simplifying distance calculations by determining the closest point on each strut via parametric projection using dot products and vector norms, thereby avoiding computationally expensive trigonometric operations (e.g., inverse cosine functions).

Due to the radius-based voxelization criterion, unit cells with sharp corners, such as nodes 2, 3, and 4 in Fig. 1g, appear with smoothly filleted edges in the voxelized representation. The relative mass density of each unit cell was calculated as the fraction of voxels occupied by solid material, obtained by dividing the number of solid voxels by the total number of voxels ($n^3$) and expressing the result as a percentage.

To generate the voxelized geometries, the Cartesian coordinates of all unit-cell vertices (nodes, Fig. 1g) were first parameterized based on the analytical expressions summarized in Supplementary Table 1. The coordinate system was defined such that its origin coincided with one corner of the cubic domain (Fig. 1c). Using these nodal coordinates and their prescribed connectivity, two input files (i.e., node and strut) were generated to define the unit cell topology. All voxelization procedures were implemented in MATLAB (R2024b, MathWorks, USA).

### Calculating the connectivity, tortuosity, and permeability of the meta-biomaterials

The connectivity of the meta-biomaterials was calculated as the ratio of the sum of the local connectivity at each node within the unit cell to the total number of nodes, following established definitions[38]. The

corresponding analytical expression used for this calculation is provided in Supplementary Note 2. The surface-to-volume ratio ($S/V$) was defined as the ratio of the total surface area of all struts within a unit cell to the corresponding unit cell volume. The empirical formulation for this metric is also detailed in Supplementary Note 2.

We defined the geometrical tortuosity (i.e., $\tau$), as the ratio of the shortest flow path length between the inlet and outlet of the unit cell to the end-to-end Euclidean length ($L_e$) of the unit cell. Specifically, the inlet and outlet were defined between nodes P1 and P16 along the vertical direction, as illustrated in Fig. 1g. The analytical expression for $\tau$ is presented in Supplementary Note 2. To obtain a more accurate estimation of tortuosity and to validate the analytical formulation, tortuosity was additionally computed using a 3D voxel-based model. For this purpose, the unit cells were voxelized and converted into 2D image stacks ($z$-stacks), as shown in Supplementary Videos 2–4. The z-stacks were subsequently merged in ImageJ to reconstruct the full 3D voxelized geometry, and tortuosity was calculated using a customized ImageJ plugin[36].

The permeability of the meta-biomaterials was evaluated numerically using the finite element software COMSOL Multiphysics (v6.1, COMSOL Inc., Sweden). For each design, the pore domain was generated by subtracting the solid voxelized unit cell from a cubic domain of side length $H$, resulting in a fully connected porous volume through which fluid could flow (Supplementary Fig. 4e, f). Fluid transport was modeled under creeping flow conditions by solving the continuity and Navier-Stokes equations. To maintain consistency with the experimental measurements, a constant volumetric flow rate of 28 mL/s was prescribed at the inlet, while atmospheric pressure was imposed at the outlet. All solid-fluid interfaces were treated as no-slip walls, and symmetry boundary conditions were applied on the four lateral faces. The fluid properties were set to those of glycerol, with a density of 1260 kg m$^{-3}$ and a dynamic viscosity of 1.49 Pa s[39]. The intrinsic permeability was subsequently calculated using Supplementary Eq. (25).

Experimental permeability measurements were conducted using a gravity-driven setup[40], in which each specimen was positioned at the bottom of a vertical standpipe aligned with the flow direction. The standpipe, with a 59 mm diameter, was filled with glycerol (VWR, USA) at room temperature, allowing the fluid to flow steadily through the specimen. The hydraulic conductivity, $K$, was determined by measuring the time ($t$) required for the glycerol level to drop from height $W_1$ to $W_2$ (Fig. S4c), according to a modified form of Darcy's law:

$$K = \frac{a}{A_m}\frac{t_m}{t}\ln\frac{W_1}{W_2} \tag{1}$$

where $a$ is the cross-sectional area of the standpipe ($a = \pi \times 29.5^2$ mm$^2$), $A_m$ is the cross-sectional area of the specimen ($A_m = 20 \times 20$ mm$^2$), $t_m$ is the specimen thickness in the flow direction ($t_m = 10$ mm), and $W_1$ and $W_2$ are the initial and final fluid heights ($W_1$ = 10.9 mm and $W_2$ = 3.5 mm), respectively. The intrinsic permeability, $k$, was then calculated from the hydraulic conductivity using[41]:

$$k = K\frac{\mu}{\rho_f g} \tag{2}$$

where $\mu$ and $\rho_f$ denote the dynamic viscosity and density of glycerol, respectively, and $g$ is the gravitational acceleration. Values of $\mu$ = 1.49 Pa s, $\rho_f = 1260$ kg m$^{-3}$, and $g$ = 9.81 m s$^{-2}$ were used in all calculations.

### Numerical homogenization modeling of the meta-biomaterials

To model the meta-biomaterials in this study, we applied periodic boundary conditions (Fig. 1b) to significantly reduce computational time. This approach is particularly useful because the real meta-biomaterials have complex microarchitectures composed of multiple unit cells oriented in different directions (i.e., $x$, $y$, and $z$). Moreover, we employed a computational homogenization technique to calculate the effective mechanical properties, including the $E_{eff}$, $G_{eff}$, and $A$. The use of this homogenization method was motivated by the high computational cost of FE modeling for such complex meta-biomaterials.

The homogenization technique is an efficient method for calculating the macroscopic mechanical properties of heterogeneous structures with microarchitectures, assuming perfect bonding between phases (e.g., between void and solid phases or between two different materials)[31,42]. In the asymptotic homogenization method, the macroscopic elasticity tensor is derived from the locally varying elasticity tensor, strain field, and prescribed strain field (Supplementary Eqs. (26–29)). This process results in a governing elasticity equation, in which the effective elasticity tensor is solved numerically by discretizing the equation using FEM to calculate the global displacement fields. Detailed descriptions of the implementation of this method can be found in ref. 5, which are based on works[42] and[31] for 2D and 3D boundary-value problems, respectively. Here, we used a customized version of the MATLAB function provided by ref. 31 with higher computational speed (MATLAB (R2024b, MathWorks, USA)).

### 3D solid FEM of the meta-biomaterials

To validate the numerical homogenization results of the 3D meta-biomaterials, we analyzed 3D solid elements of the meta-biomaterial designs using FEM via the commercial nonlinear FEM code, Abaqus, (2022, Dassault Systèmes, France). The meta-biomaterials were simulated using a quasi-static solver that accounted for geometrical nonlinearity due to the structures' complexity. Specifically, the ".step" (the standard for the exchange of product data) files of the designs, consisting of $5 \times 5 \times 5$ unit cells, were imported from SolidWorks (2022, Dassault Systèmes, France) into Abaqus. The same material properties used in the homogenization method were applied to the 3D solid FEM, considering linear isotropic behavior of the base polymer (VeroMagentaV$^{TM}$).

Two reference points were defined and kinematically coupled to all the nodes on the top and bottom surfaces of the meta-biomaterials. As a boundary condition, all the degrees of freedom at the bottom reference point were fixed (i.e., $U = U_R = 0$). The meta-biomaterials were subjected to mechanical loading by applying a uniaxial compression displacement with 1% strain. It is important to note that, due to the symmetry of the meta-biomaterials in three orthogonal directions, we only loaded the specimens along one direction, $y$, in all the 3D solid elements simulations and experiments.

The meta-biomaterials were meshed using 3D quadratic tetrahedral elements (10 nodes), known as C3D10 (Supplementary Fig. 1c). To ensure the reliability of our numerical investigations and obtain consistent results regardless of mesh size, we conducted a mesh-convergence analysis. The results indicated that the effective elastic modulus values converged within a 4% range with 1.4 million elements and an hour-long simulation time.

The engineering stress of the meta-biomaterials was calculated by dividing the reaction force obtained from the FE modeling simulations by the initial projected cross-sectional area of the specimens. The engineering strain ($\varepsilon$) was defined as the ratio of the applied displacement at the top reference point to the initial height of the meta-biomaterials. Based on these definitions, the effective elastic modulus was determined from the reaction force at the top reference point (i.e., $F_{RP_{top}}$) and the projected cross-sectional area according to the following expression:

$$E_{eff} = \frac{F_{RP_{top}}}{H^2 N_z N_x} \times \frac{1}{\epsilon} \tag{3}$$

Poisson's ratio was calculated by considering the lateral deformations of either the middle nodes or all nodes. Depending on the approach, the values of Poisson's ratios may differ slightly. Here, we assumed that the middle layers were sufficiently far from the boundary conditions (top for loading and bottom for fixed constraints) and thus calculated Poisson's ratio based on the displacement of the middle nodes/layers as follows:

$$\upsilon = \frac{-\varepsilon_x}{\varepsilon_y} = \frac{-\left(U_{x_{\text{left}}} - U_{x_{\text{right}}}\right)}{\varepsilon H N_x} \tag{4}$$

where $U_{x_{\text{left}}}$ and $U_{x_{\text{right}}}$ are the average displacements (along $x$) of the nodes of the three middle layers (Fig. 1a).

### Multi-objective optimization process for decoupling properties in the meta-biomaterials

The simultaneous regulation of ten distinct mechanical and morphometric properties in the proposed meta-biomaterials required the development of a robust multi-objective optimization framework. The computational simulations produced a dataset organized as a 44,837 × 10 matrix, denoted as Result, in which each row corresponds to a unique meta-biomaterial design and each column represents one of the ten target properties. To systematically identify pairs of designs ($i$, $j$) that exhibit isolated deviation in a single property while minimizing deviations in all others, all possible pairwise combinations of the 44,837 designs were evaluated, resulting in a permutation matrix (*Result_P*) containing 1,005,155,866 design pairs.

For each design pair *(i, j)* in *Result_P*, the relative variation of a given property was computed to normalize differences across properties with different physical units and magnitudes. This relative deviation, $D_x$, was defined as:

$$D_x = \frac{\left|x_i - x_j\right|}{\max\left(\left|x_i\right| \text{and} \left|x_j\right|\right)} \times 100 \tag{5}$$

Because evaluating all properties simultaneously for such a large dataset would require prohibitively high memory capacity, the optimization was performed separately for each target property. To isolate the effects of a specific property (e.g., Poisson's ratio), the dataset was filtered to retain only those design pairs for which the deviations in the remaining nine non-target properties were below a prescribed threshold, denoted as min $Var$. For example, when isolating Poisson's ratio, the following constraint was imposed:

$$\begin{aligned} D_E \le minVar \& D_G \le minVar \& D_A \le minVar \& D_\rho \le minVar \& D_{PS_B} \\ \le minVar \& D_\tau \le minVar \& D_{S/V} \le minVar \end{aligned} \tag{6}$$

To assess the feasibility of decoupling under different tolerance levels, min $Var$ was systematically varied across six thresholds: 5%, 10%, 15%, 20%, 25%, and 30%. The resulting filtered dataset (*Result_F*) excluded the target property (e.g., $\upsilon$) to enable evaluation of isolated variations.

To identify the most strongly decoupled pairs, *Result_F* was further refined depending on the property of interest. In the case of Poisson's ratio, candidate pairs were required to satisfy two additional criteria: (*i*) opposite signs (negative versus positive Poisson's ratio) and (*ii*) magnitudes exceeding 0.09. Accordingly, the following ranking metric was applied:

$$\left|\upsilon_i - \upsilon_j\right| \times \left|\upsilon_i\right| \times \left|\upsilon_j\right| \tag{7}$$

The filtered matrix was sorted in descending order according to Eq. (7), and the top 150 pairs that satisfied all criteria were selected as optimal candidates.

For all other properties, including elastic modulus, shear modulus, Zener ratio, pore size, relative mass density, tortuosity, and surface-to-volume ratio, a modified ranking criterion was used:

$$\left|x_i - x_j\right| \tag{8}$$

The final candidate pairs were sorted according to the values of Eqs. (7 and 8), together with the corresponding variations, property values, and geometric input parameters. From the top 150 optimized pairs, the most suitable designs were selected based on practical considerations related to 3D printing feasibility and experimental characterization. All optimization procedures were implemented in MATLAB (R2024b, MathWorks, USA).

### PolyJet 3D printing of the meta-biomaterials

The meta-biomaterials were fabricated using a multi-material PolyJet 3D printer (PolyJet J5 MediJet®, Stratasys® Ltd., USA), which operates based on a spray-based inkjet deposition process followed by ultraviolet (UV) curing. In this technique, microscopic droplets of a liquid photopolymer are selectively deposited and subsequently polymerized using UV light to form solid structures.

The commercially available photopolymer VeroMagentaV™ (RGD852, Stratasys® Ltd., USA), a relatively stiff material, was used as the structural material for all PolyJet-fabricated specimens. Owing to the geometric complexity of the meta-biomaterials, particularly those belonging to Category I, which feature re-entrant unit-cell architectures, support material was required during fabrication. A water-soluble support material, WSS™150 (Stratasys® Ltd, USA), was therefore employed.

The 3D geometries of the meta-biomaterials were exported as .STL files and imported into the printer-compatible software (GrabCAD Print, Stratasys® Ltd, USA) for build preparation and fabrication. Following printing, the specimens were immersed in tap water overnight to dissolve the support material and were subsequently air-dried in a fume hood overnight prior to further characterization.

### 2PP-based fabrication of the meta-biomaterial specimens

The meta-biomaterials at the micro-level were fabricated using 2PP. 2PP is an advanced 3D printing technique capable of fabricating very small features, from a few hundred nanometers to larger scales (centimeters) by two-photon absorption of a femtosecond laser[43,44]. The initial designs were created using SolidWorks (2022, Dassault Systèmes, France) and then exported as .STL files. These files were imported into DeScribe software (Nanoscribe, Germany) to generate General Writing Language (.gwl) files, which were subsequently used in Nanowrite software (printing software, Nanoscribe, Germany) to interface with the 2PP 3D printer for the fabrication process. The printing was carried out using a Photonic Professional GT + 3D printer from Nanoscribe.

The dip-in laser lithography (DiLL) configuration was employed, using a 10× objective featuring a numerical aperture (N.A) of 0.30. This lens was chosen based on the size of the specimens and solid/void features that needed to be accurately reproduced. A negative tone, methacrylate-based resin known as IP-Q (Nanoscribe, Germany) with a refractive index of 1.49 was used as the photoresist. The specimens were printed on silicon substrates ($25 \times 25 \times 0.7\ \text{mm}^3$, Nanoscribe, Germany) with a refractive index of 3.71 @ 780 nm.

For the stage movement during the print, we employed the piezo modality instead of the $z$-drive one. That is because the $z$-drive movement can induce micro-mechanical instability in the stage and the photoresists, potentially leading to imperfections. Given the maximum 300 μm range for the piezo mode, the overall size of the

meta-biomaterials (i.e., $1.5 \times 1.5 \times 1.5\ mm^3$), and the writing field of the 10× objective ($707.10 \times 707.10\ \mu m^2$), we stitched the meta-biomaterials into smaller blocks. To further minimize photoresist instability at the start of the print, we set the displacement velocity of the stage to $100\ \mu m\ s^{-1}$ while the maximum acceleration of the galvo scanner was programmed to $5\ V\ ms^{-2}$. After conducting multiple printing trials to optimize the printing parameters, we finalized the following settings: 100% laser power (i.e., 50 mW), a scanning speed of $30000\ \mu m\ s^{-1}$, and slicing and hatching distances of 1 μm.

To improve print quality in solid structures, we integrated a block shear angle (the angle between the stitched designs) with a specific overlap. Since the meta-biomaterials contain tilted struts, it was crucial to consider the effects of both the tilted struts and the block shear angle at the same time. A block shear angle of 40° was selected for all types of meta-biomaterials to achieve better printing quality, along with 5 μm overlaps in both vertical and longitudinal directions.

Additionally, overlaps between the segments and the number and spacing of contours were optimized to enhance printing quality. This optimization was achieved by conducting several tests on a unit cell of the meta-biomaterials (without stitching) to determine the best settings for these parameters. Based on the quality of the prints, five contours with a 1 μm spacing were selected.

Before printing, the silicon substrates were cleaned with acetone and isopropyl alcohol (IPA; both from Sigma-Aldrich, Germany) using a lint-free wipe, followed by blow drying with nitrogen. To further clean and activate the surface of the substrates, an oxygen plasma cleaner (Diener Electronic GmbH, Germany) was used at 80 W with a gas flow rate of $5\ cm^3\ min^{-1}$ and a pressure of 0.12 bar for 15 min. To enhance the adhesion between the specimens and substrates, silanization was performed by submersing the substrates into pure 3-(trimethoxysilyl) propyl methacrylate (Sigma-Aldrich, Germany) for 1 h. Silanization facilitates effective chemical bonding by making the substrate surface hydrophobic. After silanization, the specimens were washed with IPA and distilled water, followed by air-drying.

After exposing the specimens, they were immersed in propylene glycol monomethyl ether acetate (PGMEA, Sigma-Aldrich, Germany) for 1 h in a borosilicate petri dish to dissolve the unpolymerized resin. The specimens were then rinsed with IPA for 5 min to remove residual PGMEA. To further reduce capillary force-induced deformation in the structures and to enhance bonding between the specimens and silicon substrates, Novec 7100 engineered fluid (Sigma-Aldrich, Germany) was applied for 30 s, as this solvent has a lower surface tension than IPA.

### Macro-mechanical compression test

To determine the Young's modulus of VeroMagentaV™, uniaxial compression tests were performed using a mechanical testing system (LLOYD Instruments LR5K, UK) equipped with interchangeable load cells. Cylindrical specimens of VeroMagentaV™ were fabricated by PolyJet printing with dimensions of 10 mm in diameter and 15 mm in height, with three replicates tested for each condition. The samples were compressed via a 5 kN load cell at a $5\ mm\ min^{-1}$ displacement rate.

Depending on the stiffness of the specimens, different load cells were employed to ensure optimal force resolution: a 50 N load cell was used for samples 2, 3, 4, and 5, as well as for the Poisson's-ratio-isolated meta-biomaterials (P1 and P2; Fig. 5); a 100 N load cell was used for sample 1 and the relative mass density-isolated meta-biomaterial R1; and a 1000 N load cell was used for meta-biomaterial R2. All compression tests were conducted under quasi-static conditions at a constant displacement rate of $3\ mm\ min^{-1}$.

Force-displacement data acquired during testing were converted into engineering stress and engineering strain. Engineering stress was calculated by dividing the measured force by the initial projected cross-sectional area ($50 \times 50\ mm^2$ for the meta-biomaterials and $\pi \times 5.0^2\ mm^2$ for the cylindrical specimens), while engineering strain was obtained by dividing the displacement by the initial specimen height (50 mm for the meta-biomaterials and 15 mm for the cylindrical samples). The effective elastic modulus of the meta-biomaterials was determined from the linear portion of the resulting engineering stress-strain curves.

Poisson's ratio was measured by tracking lateral deformation during uniaxial compression. Specimen deformation was recorded using a digital camera (Sony E 30 mm f/3.5 Macro, Sony Group Corporation, Japan). Lateral and longitudinal displacements were extracted from the recorded videos using a customized MATLAB code. Specifically, lateral displacements were measured at three nodes in each of the three middle layers on both the left and right sides of the specimens, while longitudinal displacements were obtained from the top nodes. For strains below 2.5%, Poisson's ratio was calculated as the negative ratio of the mean lateral strain to the mean longitudinal strain.

### Meso-mechanical compression test

For uniaxial compression of the 2PP 3D-printed meta-biomaterials, we used a dynamic mechanical testing machine (MechanoCulture TX, CellScale, Canada). For this purpose, we used a 10 N load cell to compress the specimens under load-controlled mode (with a maximum force of 1 N) over a 10 s period.

### SEM and optical imaging

Prior to scanning electron microscopy (SEM), all the specimens were sputter-coated with gold at 20 mA for 20 s twice, using ±45° tilted configurations to ensure a homogeneous distribution of the gold layer, which was approximately 12 nm. SEM imaging was performed using a JEOL JSM-IT100 (Japan). The accelerating voltage and working distance for the SEM images were 10–15 kV, and 25 mm, respectively. For optical imaging of our specimens, we used a Keyence Digital Microscope VHX-6000 (Keyence, Japan).

### Statistics and reproducibility

For the experimental results, all tests were performed on $n = 3$ samples, and results are reported as mean ± standard deviation (SD). Given the type of representation of the results, the $p$-value was not reported here. The computational predictions and experimental measurements are compared descriptively to assess agreement between the model and experiments.

## Data availability

All data in the main text and the Supplementary Information are provided in the Supplementary Data files (Supplementary Videos#6–14) and Source Data file with this article. The raw data of this study are also deposited on Zenodo with corresponding https://doi.org/10.5281/zenodo.21644370. Source data are provided with this paper.

## Code availability

The customized codes developed in this study are deposited on Zenodo with corresponding https://doi.org/10.5281/zenodo.21644370.

## References

1. Yarali, E. et al. Bone cell response to additively manufactured 3D micro-architectures with controlled Poisson's ratio: auxetic vs. non-auxetic meta-biomaterials. *Acta Biomater.* **177**, 228–242 (2024).
2. Jiao, P., Mueller, J., Raney, J. R., Zheng, X. & Alavi, A. H. Mechanical metamaterials and beyond. *Nat. Commun.* **14**, 6004 (2023).
3. Pahlavani, H. et al. Deep learning for size-agnostic inverse design of random-network 3D printed mechanical metamaterials. *Adv. Mater.* **36**, 2303481 (2024).
4. Lee, Y. et al. A seamless auxetic substrate with a negative Poisson's ratio of– 1. *Nat. Commun.* **15**, 7146 (2024).
5. Kadic, M., Milton, G. W., van Hecke, M. & Wegener, M. 3D metamaterials. *Nat. Rev. Phys.* **1**, 198–210 (2019).

6. Gao, Z. et al. Damage-programmable design of metamaterials achieving crack-resisting mechanisms seen in nature. *Nat. Commun.* **15**, 7373 (2024).
7. Ha, C. S. et al. Rapid inverse design of metamaterials based on prescribed mechanical behavior through machine learning. *Nat. Commun.* **14**, 5765 (2023).
8. Park, J., Noh, J., Shin, J., Gu, G. X. & Rho, J. Investigating static and dynamic behaviors in 3D chiral mechanical metamaterials by disentangled generative models. *Adv. Funct. Mater.* **35**, 2412901 (2024).
9. Yu, P. et al. A multi-step auxetic metamaterial with instability regulation. *Int. J. Solids Struct.* **305**, 113040 (2024).
10. Callens, S. J., Arns, C. H., Kuliesh, A. & Zadpoor, A. A. Decoupling minimal surface metamaterial properties through multi-material hyperbolic tilings. *Adv. Funct. Mater.* **31**, 2101373 (2021).
11. Guo, Y. et al. Minimal surface-based materials for topological elastic wave guiding. *Adv. Funct. Mater.* **32**, 2204122 (2022).
12. Zadpoor, A. A. Additively manufactured porous metallic biomaterials. *J. Mater. Chem. B* **7**, 4088–4117 (2019).
13. Hashin, Z. & Shtrikman, S. A variational approach to the theory of the elastic behaviour of multiphase materials. *J. Mech. Phys. Solids* **11**, 127–140 (1963).
14. Wu, S., Luo, Z., Li, Z., Liu, S. & Zhang, L.-C. Topological design of pentamode metamaterials with additive manufacturing. *Comput. Methods Appl. Mech. Eng.* **377**, 113708 (2021).
15. Hu, X., Tan, T., Wang, B. & Yan, Z. A reprogrammable mechanical metamaterial with origami functional-group transformation and ring reconfiguration. *Nat. Commun.* **14**, 6709 (2023).
16. Li, T. & Li, Y. 3D tiled auxetic metamaterial: a new family of mechanical metamaterial with high resilience and mechanical hysteresis. *Adv. Mater.* **36**, 2309604 (2024).
17. Wang, L. et al. Multistep and elastically stable mechanical metamaterials. *J. Appl. Mech.* **91**, 111002 (2024).
18. Yarali, E., Zadpoor, A. A., Staufer, U., Accardo, A. & Mirzaali, M. J. Auxeticity as a mechanobiological tool to create meta-biomaterials. *ACS Appl. Bio Mater.* **6**, 2562–2575 (2023).
19. Do, Q. T., Nguyen, C. H. P. & Choi, Y. Homogenization-based optimum design of additively manufactured Voronoi cellular structures. *Addit. Manuf.* **45**, 102057 (2021).
20. Meier, T. et al. Obtaining auxetic and isotropic metamaterials in counterintuitive design spaces: an automated optimization approach and experimental characterization. *npj Comput. Mater.* **10**, 3 (2024).
21. Flamourakis, G. et al. Laser-made 3D auxetic metamaterial scaffolds for tissue engineering applications. *Macromol. Mater. Eng.* **305**, 2000238 (2020).
22. Kolken, H. M. et al. Rationally designed meta-implants: a combination of auxetic and conventional meta-biomaterials. *Mater. Horiz.* **5**, 28–35 (2018).
23. Munding, N. et al. Bio-metamaterials for mechano-regulation of mesenchymal stem cells. *Adv. Funct. Mater.* **34**, 2301133 (2023).
24. Dudek, K. K. et al. Micro-scale mechanical metamaterial with a controllable transition in the Poisson's ratio and band gap formation. *Adv. Mater.* **35**, 2210993 (2023).
25. Mirzaali, M. J., Pahlavani, H., Yarali, E. & Zadpoor, A. Non-affinity in multi-material mechanical metamaterials. *Sci. Rep.* **10**, 11488 (2020).
26. Tancogne-Dejean, T. & Mohr, D. Elastically-isotropic truss lattice materials of reduced plastic anisotropy. *Int. J. Solids Struct.* **138**, 24–39 (2018).
27. Zheng, X., Zhang, X., Chen, T. T. & Watanabe, I. Deep learning in mechanical metamaterials: from prediction and generation to inverse design. *Adv. Mater.* **35**, 2302530 (2023).
28. Abu-Mualla, M. & Huang, J. Inverse design of 3D cellular materials with physics-guided machine learning. *Mater. Des.* **232**, 112103 (2023).
29. Zheng, X., Chen, T.-T., Guo, X., Samitsu, S. & Watanabe, I. Controllable inverse design of auxetic metamaterials using deep learning. *Mater. Des.* **211**, 110178 (2021).
30. Chen, W. et al. Stiff isotropic lattices beyond the Maxwell criterion. *Sci. Adv.* **5**, eaaw1937 (2019).
31. Dong, G., Tang, Y. & Zhao, Y. F. A 149 line homogenization code for three-dimensional cellular materials written in matlab. *J. Eng. Mater. Technol.* **141**, 011005 (2019).
32. Mirzaali, M., Pahlavani, H., Yarali, E. & Zadpoor, A. Non-affinity in multi-material mechanical metamaterials. *Sci. Rep.* **10**, 11488 (2020).
33. Cheng, X. et al. Design and mechanical characteristics of auxetic metamaterial with tunable stiffness. *Int. J. Mech. Sci.* **223**, 107286 (2022).
34. Kolken, H. et al. Mechanical performance of auxetic meta-biomaterials. *J. Mech. Behav. Biomed. Mater.* **104**, 103658 (2020).
35. Ostanin, I., Ovchinnikov, G., Tozoni, D. C. & Zorin, D. A parametric class of composites with a large achievable range of effective elastic properties. *J. Mech. Phys. Solids* **118**, 204–217 (2018).
36. Roque, W. L. & Costa, R. R. A plugin for computing the pore/grain network tortuosity of a porous medium from 2D/3D MicroCT image. *Appl. Comput. Geosci.* **5**, 100019 (2020).
37. Graczyk, K. M. & Matyka, M. Predicting porosity, permeability, and tortuosity of porous media from images by deep learning. *Sci. Rep.* **10**, 21488 (2020).
38. Mirzaali, M. J., Pahlavani, H. & Zadpoor, A. Auxeticity and stiffness of random networks: lessons for the rational design of 3D printed mechanical metamaterials, *Appl. Phys. Lett.* **115**, 021901 (2019).
39. Andreini, N., Epely-Chauvin, G. & Ancey, C. Internal dynamics of Newtonian and viscoplastic fluid avalanches down a sloping bed. *Phys. Fluids* **24**, 053101 (2012).
40. Pennella, F. et al. A survey of methods for the evaluation of tissue engineering scaffold permeability. *Ann. Biomed. Eng.* **41**, 2027–2041 (2013).
41. Bear, J. *Dynamics of Fluids in Porous Media* (Courier Corporation, 2013).
42. Andreassen, E. & Andreasen, C. S. How to determine composite material properties using numerical homogenization. *Comput. Mater. Sci.* **83**, 488–495 (2014).
43. Wang, W. et al. Two-photon polymerization-based 3D microscaffolds toward biomedical devices. *Chem. Eng. J.* **493**, 152469 (2024).
44. Lyu, X. et al. Capillary trapping of various nanomaterials on additively manufactured scaffolds for 3D micro-/nanofabrication. *Nat. Commun.* **15**, 6693 (2024).


## Acknowledgements

We sincerely acknowledge the Faculty of Mechanical Engineering (ME, TU Delft) for supporting this project through the Cohesion grant "Biomimetic-meta-implants" awarded to M.J.M. and A.A. Moreover, the authors (A. A. Zadpoor and M. J. Mirzaali) acknowledge the financial support from the European Union Horizon Europe research and innovation programme under the Marie Skłodowska-Curie (MSCA) grant agreement No 101120290 (GAP).

## Author contributions

M.J.M., A.A., and A.A.Z. conceptualized the project. M.J.M., A.A., A.A.Z., and U.S. supervised the project. E.Y., M.J.M., A.A., A.A.Z., U.S., and L.E.F. conducted the investigation. E.Y. performed the computational design of the meta-biomaterials and their multi-objective optimization. R.M. performed the COMSOL modeling to calculate permeability. E.Y.

performed experimental evaluations, including PolyJet and two-photon polymerization 3D printing, mechanical compression testing, permeability measurement, and statistical analysis. A.A.S. assisted with 3D printing and compression tests during revision. E.Y. wrote the manuscript, and M.J.M., A.A., A.A.Z., and U.S. reviewed and revised it.

## Competing interests
The authors declare no competing interests.

## Additional information
**Supplementary information** The online version contains supplementary material available at https://doi.org/10.1038/s41467-026-77121-y.

**Correspondence** and requests for materials should be addressed to Ebrahim Yarali, Angelo Accardo or Mohammad J. Mirzaali.

**Peer review information** *Nature Communications* thanks Mohammad Mirkhalaf and the other anonymous reviewer(s) for their contribution to the peer review of this work. A peer review file is available.

**Reprints and permissions information** is available at http://www.nature.com/reprints

**Publisher's note** Springer Nature remains neutral with regard to jurisdictional claims in published maps and institutional affiliations.

**Open Access** This article is licensed under a Creative Commons Attribution-NonCommercial-NoDerivatives 4.0 International License, which permits any non-commercial use, sharing, distribution and reproduction in any medium or format, as long as you give appropriate credit to the original author(s) and the source, provide a link to the Creative Commons licence, and indicate if you modified the licensed material. You do not have permission under this licence to share adapted material derived from this article or parts of it. The images or other third party material in this article are included in the article's Creative Commons licence, unless indicated otherwise in a credit line to the material. If material is not included in the article's Creative Commons licence and your intended use is not permitted by statutory regulation or exceeds the permitted use, you will need to obtain permission directly from the copyright holder. To view a copy of this licence, visit http://creativecommons.org/licenses/by-nc-nd/4.0/.

© The Author(s) 2026